

Tracing the cold and warm physico-chemical structure of deeply embedded protostars: IRAS 16293–2422 vs. VLA 1623–2417

N. M. Murillo¹, E. F. van Dishoeck^{1,2}, M. H. D. van der Wiel^{3,4}, J. K. Jørgensen³, M. N. Drozdovskaya^{1,5},
H. Calcutt³, and D. Harsono¹

¹ Leiden Observatory, Leiden University, PO Box 9513, 2300 RA Leiden, The Netherlands
e-mail: nmurillo@strw.leidenuniv.nl

² Max-Planck-Institut für extraterrestrische Physik, Giessenbachstraße 1, 85748 Garching bei München, Germany

³ Centre for Star and Planet Formation, Niels Bohr Institute & Natural History Museum of Denmark, University of Copenhagen, Øster Voldgade 5–7, 1350 Copenhagen K., Denmark

⁴ ASTRON, the Netherlands Institute for Radio Astronomy, Postbus 2, 7990 AA Dwingeloo, The Netherlands

⁵ Center for Space and Habitability (CSH), University of Bern, Sidlerstrasse 5, 3012 Bern, Switzerland

Received 5 August 2017 / Accepted 29 April 2018

ABSTRACT

Context. Much attention has been placed on the dust distribution in protostellar envelopes, but there are still many unanswered questions regarding the physico-chemical structure of the gas.

Aims. Our aim is to start identifying the factors that determine the chemical structure of protostellar regions, by studying and comparing low-mass embedded systems in key molecular tracers.

Methods. The cold and warm chemical structures of two embedded Class 0 systems, IRAS 16293–2422 and VLA 1623–2417 were characterized through interferometric observations. DCO⁺, N₂H⁺, and N₂D⁺ were used to trace the spatial distribution and physics of the cold regions of the envelope, while c-C₃H₂ and C₂H from models of the chemistry are expected to trace the warm (UV-irradiated) regions.

Results. The two sources show a number of striking similarities and differences. DCO⁺ consistently traces the cold material at the disk-envelope interface, where gas and dust temperatures are lowered due to disk shadowing. N₂H⁺ and N₂D⁺, also tracing cold gas, show low abundances toward VLA 1623–2417, but for IRAS 16293–2422, the distribution of N₂D⁺ is consistent with the same chemical models that reproduce DCO⁺. The two systems show different spatial distributions c-C₃H₂ and C₂H. For IRAS 16293–2422, c-C₃H₂ traces the outflow cavity wall, while C₂H is found in the envelope material but not the outflow cavity wall. In contrast, toward VLA 1623–2417 both molecules trace the outflow cavity wall. Finally, hot core molecules are abundantly observed toward IRAS 16293–2422 but not toward VLA 1623–2417.

Conclusions. We identify temperature as one of the key factors in determining the chemical structure of protostars as seen in gaseous molecules. More luminous protostars, such as IRAS 16293–2422, will have chemical complexity out to larger distances than colder protostars, such as VLA 1623–2417. Additionally, disks in the embedded phase have a crucial role in controlling both the gas and dust temperature of the envelope, and consequently the chemical structure.

Key words. astrochemistry – stars: formation – stars: low-mass – stars: individual: IRAS 16293–2422 – methods: observational – stars: individual: VLA 1623–2417

1. Introduction

While there is a well-established outline of the physical evolution of protostellar systems (Evans 1999; Dunham et al. 2014; Li et al. 2014; Reipurth et al. 2014), there are still many questions regarding the physico-chemical structure of these systems. Several studies point out the chemical richness and diversity of young embedded protostars, most notably in the Class 0 stage, ranging from simple molecules to carbon chains and complex organics (see reviews by Herbst & van Dishoeck 2009; Caselli & Ceccarelli 2012; Sakai & Yamamoto 2013). In contrast, some other protostellar systems show much less chemical complexity (e.g., Jørgensen et al. 2005b; Maret et al. 2006; Öberg et al. 2014; Lindberg et al. 2014b, 2016, 2017; Fayolle et al. 2015; Bergner et al. 2017), a situation made more extreme when some starless cores have stronger molecular line emissions than the already formed protostars (e.g., Bergman et al. 2011; Bacmann et al. 2012; Friesen et al. 2014). It is interesting to explore the chemical

structure and evolution of early stage protostars and what physical quantities dictate the resulting chemical structure as observed in the gas phase.

The chemical fingerprint generated in the early embedded stages of star formation may be transmitted to the later stages and eventually the protoplanetary disk, where planets and comets are formed (e.g., Aikawa et al. 1999; Aikawa & Herbst 1999; Visser et al. 2009, 2011; Hincelin et al. 2013; Drozdovskaya et al. 2014; Willacy et al. 2015; Yoneda et al. 2016). Which factors then generate a protostellar system's fingerprint? Protostellar cores may inherit their chemical composition from the parent clouds that eventually collapse to form protostars (e.g., Visser et al. 2009, 2011; Aikawa et al. 2012; Furuya et al. 2012; Tassis et al. 2012; Hincelin et al. 2016). It would then seem likely that protostars from the same parent cloud would have a similar chemical composition. However, this would require the cloud to have a homogeneous composition, which is not always the case (Bergman et al. 2011). Instead, other mechanisms

could alter the chemical fingerprint. Turbulence and large-scale motions could stir the gas and dust of the cloud core around, moving material from the outer region of the core closer to the warmer regions of the system, kick-starting chemical reactions and producing enhancements of selected species. Formation of more complex chemical species is likely to occur through grain-surface reactions (i.e., on ice and dust surfaces) instead of in the gas-phase, and such reactions proceed faster at higher dust temperatures which increases the mobility of radicals (Garrod & Herbst 2006). If material near the outflow cavities is warmer than elsewhere in the envelope, this could generate pockets of chemically rich ices that, once heated above the sublimation temperature, would be released into the gas-phase (Drozdovskaya et al. 2015). Moreover, UV radiation can photodissociate CO and create free atomic carbon that leads to efficient formation of carbon-bearing molecules. UV irradiation, together with age and variations in accretion rates, would also produce different outcomes, even with the same initial ingredients. In addition, simple warm-chemistry molecules can be the precursors to more complex molecules (Sakai & Yamamoto 2013).

The physical evolution of the individual protostars, for example, the collapse time and structure, will also impact the chemical fingerprint. An important consideration regarding the physical structure is that disks may have formed already in the early stages, as shown by recent observations (e.g., Tobin et al. 2012; Murillo et al. 2013; Harsono et al. 2014; Codella et al. 2014; Lindberg et al. 2014a; Yen et al. 2017). Not only do disks provide a high density long-lived reservoir preventing molecules from falling into the star, but they also affect the thermal structure of their surroundings. Thus, the disk-envelope interface and the envelope itself must be studied (Murillo et al. 2015; Persson et al. 2016). The disk-envelope interface and the outer envelope of embedded systems are traced by cold-chemistry molecules, since these regions are usually shielded from heating by the central protostar (van Dishoeck et al. 1995; Jørgensen et al. 2004, 2005a; Sakai et al. 2014b; Murillo et al. 2015). Through the study of molecules sensitive to temperature, we can then understand the structure of embedded protostellar systems.

Aiming to explore the chemical evolution of the earliest embedded protostellar systems – Class 0 – we compare two systems from ρ Ophiuchus ($d \sim 120$ pc; Loinard et al. 2008), IRAS 16293–2422 and VLA 1623–2417 (Fig. 1), separated by a projected distance of 2.8 pc. Recent measurements to these two systems place IRAS 16293–2422 at a distance of 141 ± 30 pc (Dzib et al. 2018) and VLA 1623–2417 at 137.3 ± 1.2 pc (Ortiz-León et al. 2017). However, for ease of comparison with previous work, we adopt the distance of 120 pc for both sources. Most previous studies of IRAS 16293–2422 and VLA 1623–2417 were based on single-dish observations. The advent of the Atacama Large Millimeter/submillimeter Array (ALMA) now allows chemical studies on 100 AU scales that spatially resolve the different physical components of the system.

IRAS 16293–2422 (hereafter IRAS 16293) is a widely studied multiple system, located in L1689N, with a complicated outflow structure being driven by source A (Stark et al. 2004; Yeh et al. 2008; Loinard et al. 2013; Kristensen et al. 2013; Girart et al. 2014). IRAS 16293 A and B, separated by about 620 AU (Fig. 1), have different inclination angles, with the disk-like structure of A being inclined, and B being oriented face-on with respect to the line of sight (Pineda et al. 2012; Jørgensen et al. 2016). Due to the different inclination angles, it is difficult to determine whether these systems are at the same evolutionary stage or not (Murillo et al. 2016). Both components are chemically rich but show

differences in structure (Bottinelli et al. 2004; Bisschop et al. 2008; Jørgensen et al. 2011).

VLA 1623–2417 (hereafter VLA 1623) is a triple protostellar system, located in L1688 (ρ Oph A), mostly studied for its prominent outflow in the region (André et al. 1990; Caratti o Garatti et al. 2006). The three components of the system, VLA 1623 A, B, and W are separated by 132 and 1200 AU (Fig. 1), respectively, have similar inclination angles, and have also been found to be at different evolutionary stages (Murillo & Lai 2013; Murillo et al. 2013). VLA 1623 has been shown to be largely line poor in single-dish studies (Garay et al. 2002; Jørgensen et al. 2004; Bergman et al. 2011; Friesen et al. 2014).

In this paper, we present observations of DCO^+ , N_2H^+ , N_2D^+ , $c\text{-C}_3\text{H}_2$, and C_2H toward IRAS 16293 and VLA 1623, using ALMA, the Submillimeter Array (SMA; Ho et al. 2004), and the Atacama Pathfinder Experiment (APEX; Güsten et al. 2006). DCO^+ , N_2H^+ , and N_2D^+ are known to be good tracers of cold gas where CO is frozen out. $c\text{-C}_3\text{H}_2$ and C_2H are usually seen in photon-dominated regions (PDRs) such as the Orion Bar (Pety et al. 2007; van der Wiel et al. 2009; Nagy et al. 2015) and the Horsehead Nebula (Cuadrado et al. 2015; Guzmán et al. 2015), with both species located at the irradiated, and thus warmer, edge of these regions. $c\text{-C}_3\text{H}_2$ and C_2H could thus be expected to trace the (UV-irradiated) outflow cavity walls, although both species have also been found just outside the disk-envelope interface (Sakai et al. 2014a). Besides mapping their distributions, multiple lines from a single molecule can also be used to trace physical conditions such as temperature and density (van Dishoeck et al. 1993; Evans 1999; van der Tak et al. 2007; Shirley 2015) and the current dataset allows this to be done for several species.

Details of the observations with ALMA, SMA, and APEX are described in Sect. 2. Section 3 describes the spatial distribution of each molecule for both systems. The observations are compared to chemical models and physical parameters are derived in Sect. 4. Sections 5 and 6 compare both systems studied here with other objects found in literature and place the results of our work in context.

2. Observations

2.1. IRAS 16293–2422

IRAS 16293 was targeted in the Protostellar Interferometric Line Survey (PILS) program (Project-ID: 2013.1.00278.S; PI: Jes K. Jørgensen; Jørgensen et al. 2016), an ALMA Cycle 2 unbiased spectral survey in Band 7, using both the 12 m array and the Atacama Compact Array (ACA). The spectral setup covers a frequency range from 329.147 to 362.896 GHz, and provides a velocity resolution of 0.2 km s^{-1} . The phase center was $\alpha_{J2000} = 16:32:22.72$; $\delta_{J2000} = -24:28:34.3$, set to be equidistant from the two sources A and B at $v_{\text{lsr}} = 3.1$ and 2.7 km s^{-1} (Jørgensen et al. 2011), respectively. The resulting (u, v) coverage of the combined 12 m array and the ACA observations are sensitive to the distribution of material with an extent of up to $13''$ and a circular synthesized beam of $0.5''$. A detailed description of the observations and reduction is given in Jørgensen et al. (2016). Many complex molecules detected in this survey (e.g., Coutens et al. 2016; Jørgensen et al. 2016; Lykke et al. 2017) show relatively compact emission peaking close to the location of the two protostars. This work focuses on a few of the molecules detected in the spectral survey that show extended emission, namely, DCO^+ , $c\text{-C}_3\text{H}_2$, and C_2H . Several transitions of $c\text{-C}_3\text{H}_2$ are present throughout the frequency range of PILS,

Table 1. Summary of line observations.

Line	Transition	ν (GHz)	$\log_{10} A_{ij}$	E_{up} (K)	IRAS 16293–2422		VLA 1623–2417	
					Peak intensity (mJy beam ⁻¹)	Line width (km s ⁻¹)	Peak intensity (mJy beam ⁻¹)	Line width (km s ⁻¹)
ALMA								
c-C ₃ H ₂	6 _{0,6} –5 _{1,5}	217.822148	–3.23	38.61	194	0.5
c-C ₃ H ₂	5 _{5,0} –4 _{4,1}	349.26400	–2.78	48.98	240 ^a	0.5
c-C ₃ H ₂	10–9 ^b	351.78158	–2.61	96.49	410 ^a	0.6
c-C ₃ H ₂	9–8 ^c	351.96597	–2.67	93.34	350 ^a	0.6
c-C ₃ H ₂	8 _{2,6} –7 _{3,5}	352.18554	–2.76	86.93	90 ^a	0.6
c-C ₃ H ₂	8 _{3,6} –7 _{2,5}	352.19364	–2.76	86.93	200 ^a	0.6
C ₂ H	4–3 $J = 9/2$ – $7/2$ $F = 5$ – 4	349.33771	–3.88	41.91	170	0.6
C ₂ H	4–3 $J = 9/2$ – $7/2$ $F = 4$ – 3	349.33899	–3.89	41.91	140	0.6
C ₂ H	4–3 $J = 7/2$ – $5/2$ $F = 4$ – 3	349.39927	–3.90	41.93	140	0.6
C ₂ H	4–3 $J = 7/2$ – $5/2$ $F = 3$ – 2	349.40067	–3.92	41.93	110	0.6
DCO ⁺	3–2	216.11258	–2.62	20.74	90	0.7
DCO ⁺	5–4	360.16978	–2.42	51.86	10	1.0	290	0.7
N ₂ D ⁺	3–2	231.32166	–2.66	22.20	<8.58 ^d	...
N ₂ H ⁺	4–3	372.67251	–2.51	44.71	<94.9 ^d	...
SMA								
DCO ⁺	3–2	216.11258	–2.62	20.74	1800	1.0
N ₂ D ⁺	3–2	231.32166	–2.66	22.20	1700	2.0
APEX (T_{mb})								
C ₂ H	4–3 $J = 9/2$ – $7/2$ $F = 5$ – 4	349.33771	–3.88	41.91	0.96 K	0.7
C ₂ H	4–3 $J = 9/2$ – $7/2$ $F = 4$ – 3	349.33899	–3.89	41.91	0.62 K	0.7
C ₂ H	4–3 $J = 7/2$ – $5/2$ $F = 4$ – 3	349.39927	–3.90	41.93	0.68 K	0.7
C ₂ H	4–3 $J = 7/2$ – $5/2$ $F = 3$ – 2	349.40067	–3.92	41.93	0.34 K	0.7
DCO ⁺	3–2	216.11258	–2.62	20.74	4.8 K	0.8
DCO ⁺	5–4	360.16978	–2.42	51.86	2.2 K	0.8

Notes. ^(a)c-C₃H₂ peak intensities and line widths taken from the south peak where there is no line confusion. ^(b)Blended 10_{0,10}–9_{1,9} and 10_{1,10}–9_{0,9} transitions of c-C₃H₂. ^(c)Blended 9_{1,8}–8_{2,7} and 9_{2,8}–8_{1,7} transitions of c-C₃H₂. ^(d)1 σ noise level of N₂D⁺ and N₂H⁺ in 0.02 km s⁻¹ channel.

References. All rest frequencies were taken from the Cologne Database for Molecular Spectroscopy (CDMS; Endres et al. 2016). The c-C₃H₂ entry was based on Bogey et al. (1987) with transition frequencies important for our survey from Bogey et al. (1986) and from Spezzano et al. (2012). The CCH entry is based on Padovani et al. (2009) with additional important data from Müller et al. (2000) and Sastry et al. (1981). The DCO⁺ and N₂H⁺ entries are based on Caselli & Dore (2005) and on Cazzoli et al. (2012), respectively. Information on the N₂D⁺ rest frequency was taken from Pagani et al. (2009a).

however for this work, only five transitions with strong observed emission were chosen in the 349–352 GHz frequency range. For all molecules, the combined 12 m array and ACA data cubes are used. The typical RMS noise is about 7–10 mJy beam⁻¹ per 0.2 km s⁻¹ channel, and the flux calibration uncertainty is ~5% (Jørgensen et al. 2016). Transitions and line frequencies of the molecular species used in this work are listed in Table 1, as well as the peak intensities and line widths. In Table A.1 we list further details of the observations, such as UV-baseline range and largest angular scale recovered in the observations.

Since the PILS survey did not cover lines of N₂D⁺ 3–2 or DCO⁺ 3–2, we include here the observations of these two molecules from a spectral line survey with the SMA (Jørgensen et al. 2011). The phase center was $\alpha_{J2000} = 16:32:22.91$; $\delta_{J2000} = -24:28:35.5$. For DCO⁺ 3–2, the beam size is 5.5'' \times 3.2'' (PA = 17.7°), while for N₂D⁺ 3–2 the beam size is 4.0'' \times 2.4'' (PA = -1.0°). The RMS noise is 0.24 Jy beam⁻¹ for a 0.56 km s⁻¹ channel width for DCO⁺, and 0.06 Jy beam⁻¹ for a channel width of 1.1 km s⁻¹ for N₂D⁺. Further details on the reduction and analysis are given in Jørgensen et al. (2011). These data are considered in order to directly compare the cold chemistry of IRAS 16293 with that of VLA 1623. Additionally, two transitions of DCO⁺ are needed to derive temperature and density from line ratios.

2.2. VLA 1623–2417

VLA 1623 was observed with ALMA in Cycle 0 using Band 6, with phase center $\alpha_{J2000} = 16:26:26.419$; $\delta_{J2000} = -24:24:29.988$. The spectral set-up was configured to observe DCO⁺ 3–2 and N₂D⁺ 3–2 together with C¹⁸O 2–1 and ¹²CO 2–1, providing a velocity resolution of 0.0847 km s⁻¹ and a synthesized beam size of 0.85'' \times 0.56'' (PA = -83.8°). DCO⁺ 3–2 data from the Cycle 0 observations were previously presented in Murillo et al. (2015) and are added to this work for completeness in the comparison of both systems. The data reduction results of C¹⁸O and ¹²CO can be found in Murillo et al. (2013) and Santangelo et al. (2015).

ALMA Cycle 2 observations of VLA 1623 were carried out in Bands 6 and 7, with phase center $\alpha_{J2000} = 16:26:26.390$; $\delta_{J2000} = -24:24:30.688$. Baseline and frequency ranges are listed in Table A.1.

The Cycle 2 Band 6 spectral setup covered DCO⁺ 3–2, C¹⁸O 3–2, ¹³CO 3–2, and c-C₃H₂ 6_{0,6}–5_{1,5} together with continuum. Data calibration was done with J1733–1304 and J1517–2422 for bandpass, J1625–2527 for gain calibration, and J1517–243, J1733–130, Ceres, Mars, and Titan were observed for flux calibration. The spectral windows with line emission have bandwidths of 62 MHz each, while for continuum the total bandwidth is of 8 GHz. These observations were carried out

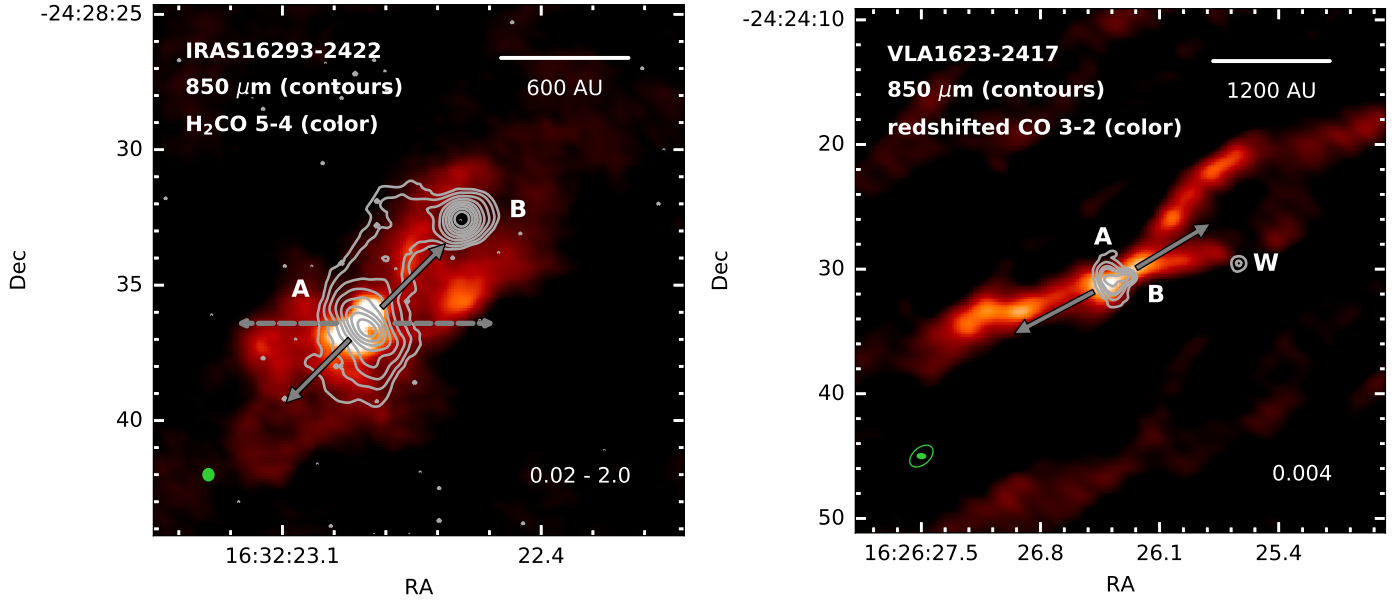


Fig. 1. Continuum at $850\ \mu\text{m}$ (contours) for both systems; IRAS 16293–2422 (*left panel*) and VLA 1623–2417 (*right panel*), overlaid on intensity integrated H_2CO ($0\text{--}60\ \text{km s}^{-1}$; color scale) and redshifted CO ($4\text{--}15\ \text{km s}^{-1}$; color scale), respectively. The green ellipses on the *bottom left panel* indicate the beam of the observations. For the *right panel*, the empty ellipse is the beam of the CO observations. For VLA 1623–2417, contours are in steps of 3, 8, 15, 20, and 50σ , with $\sigma = 0.004\ \text{Jy beam}^{-1}$. For IRAS 16293–2422, the levels are logarithmically spaced between 0.02 and $2\ \text{Jy beam}^{-1}$, and highlight the ridge that spans between sources A and B. The arrows indicate the direction of red- and blue-shifted outflows from source A in each system.

with both the Total power, ACA, and 12 m arrays, for a total of four configurations. Two configurations of the 12 m array, C35-5 ($25 \sim 1000\ \text{m}$) and C34-1 ($10 \sim 350\ \text{m}$), were used to bridge the gap between the 12 m and ACA array observations. Cycle 2 Band 6 ACA observations of DCO^+ were presented in [Murillo et al. \(2015\)](#) and are only included here for visual comparison. The 12 m and ACA C^{18}O and ^{13}CO observations from Cycle 2 Band 6 will be treated in a future publication. In this work, we focus only on the 12 m array $\text{c-C}_3\text{H}_2\ 6_{0,6}\text{--}5_{1,5}$ observations from Cycle 2 Band 6 data. The C35-5 configuration provides an angular and velocity resolution of $0.45'' \times 0.25''$ ($\text{PA} = 86.3^\circ$) and $0.0208\ \text{km s}^{-1}$, respectively, with a typical RMS noise of $7\ \text{mJy beam}^{-1}$. The C34-1 configuration results in an angular resolution of $1.60'' \times 0.88''$ ($\text{PA} = 83.8^\circ$) with a channel width of $0.0208\ \text{km s}^{-1}$ and a typical RMS noise of $20\ \text{mJy beam}^{-1}$.

Band 7 observations, with a spectral set-up covering $\text{N}_2\text{H}^+\ 5\text{--}4$, $\text{DCO}^+\ 5\text{--}4$, and $\text{H}_2\text{D}^+\ 1_{1,0}\text{--}1_{1,1}$ as well as continuum with only the 12 m array, provided a spectral and angular resolution of $0.025\ \text{km s}^{-1}$ and $0.88'' \times 0.56''$ ($\text{PA} = -86.6^\circ$), respectively. The spectral windows with line emission have a total bandwidth of 62 MHz each, and continuum has a total bandwidth of 4 GHz. Total observing time was 0.9 h with a 46% duty cycle, using 34 antennas and a maximum baseline of 350 m. Data calibration was done with J1517–2422, J1625–2527, and Titan for bandpass, gain and flux calibration, respectively. DCO^+ was detected with a noise of $26\ \text{mJy beam}^{-1}$ per $0.025\ \text{km s}^{-1}$. The system temperature was relatively high for the spectral windows containing N_2H^+ and H_2D^+ , causing the noise to be of about $95\ \text{mJy beam}^{-1}$ per $0.025\ \text{km s}^{-1}$ velocity channel, despite flagging the antennas with the highest system temperature.

In this work, we focus on the $\text{DCO}^+\ 3\text{--}2$ and $\text{N}_2\text{D}^+\ 3\text{--}2$ lines from the Cycle 0 12 m array observations, in addition to $\text{c-C}_3\text{H}_2\ 6_{0,6}\text{--}5_{1,5}$, $\text{DCO}^+\ 5\text{--}4$, $\text{N}_2\text{H}^+\ 5\text{--}4$, and $\text{H}_2\text{D}^+\ 1_{1,0}\text{--}1_{1,1}$ 12 m array observations from Cycle 2. Line transitions and

frequencies, together with peak intensities and line widths are listed in Table 1.

Additionally, single-dish APEX observations in the ON/OFF mode were carried out on 22 and 24 October, 2016 using the heterodyne instrument SheFI ([Belitsky et al. 2006](#); [Vassilev et al. 2008](#)) with Bands APEX-1 ($213\text{--}275\ \text{GHz}$) and APEX-2 ($267\text{--}378\ \text{GHz}$), targeting $\text{DCO}^+\ 3\text{--}2$ and $5\text{--}4$, as well as $\text{C}_2\text{H}\ 4\text{--}3$. These observations were taken to compare the location of C_2H in both VLA 1623 and IRAS 16293, as well as to have a separate verification and comparison of the physical parameters derived from ALMA observations and single-dish. Several transitions of NO and HCN were detected, both of which can form in gas and surface reactions, whereas N_2H^+ and N_2D^+ only form in the gas. NO and HCN are not analyzed any further in this work. The observations were centered on VLA 1623 A ($\alpha_{J2000} = 16:26:26.390$; $\delta_{J2000} = -24:24:30.688$). The typical RMS noise was 100 mK for APEX-1 and between 50 and 80 mK for APEX-2 in $0.1\ \text{km s}^{-1}$ channels. Peak temperatures (T_{mb}) and line widths for Gaussian fits to the single dish lines are listed in Table 1. The typical calibration uncertainties are about 10% for the APEX SheFI instruments in the 230 and 345 GHz Bands. For APEX-1 and APEX-2 observations, the HPBW is $28.7''$ and $18''$, respectively. The main beam efficiencies used are $\eta_{\text{mb}} = 0.75$ at 230 GHz, and $\eta_{\text{mb}} = 0.73$ at 345 GHz.

3. Results

3.1. IRAS 16293–2422

The molecules $\text{c-C}_3\text{H}_2$, C_2H , and DCO^+ from the PILES spectral survey ([Jørgensen et al. 2016](#)) are considered here, together with DCO^+ and N_2D^+ from the SMA spectral survey ([Jørgensen et al. 2011](#)). The PILES survey images are obtained from the combined 12 m array and ACA, which picks up the small and large scale emission from scales less than $13''$. The peak intensities

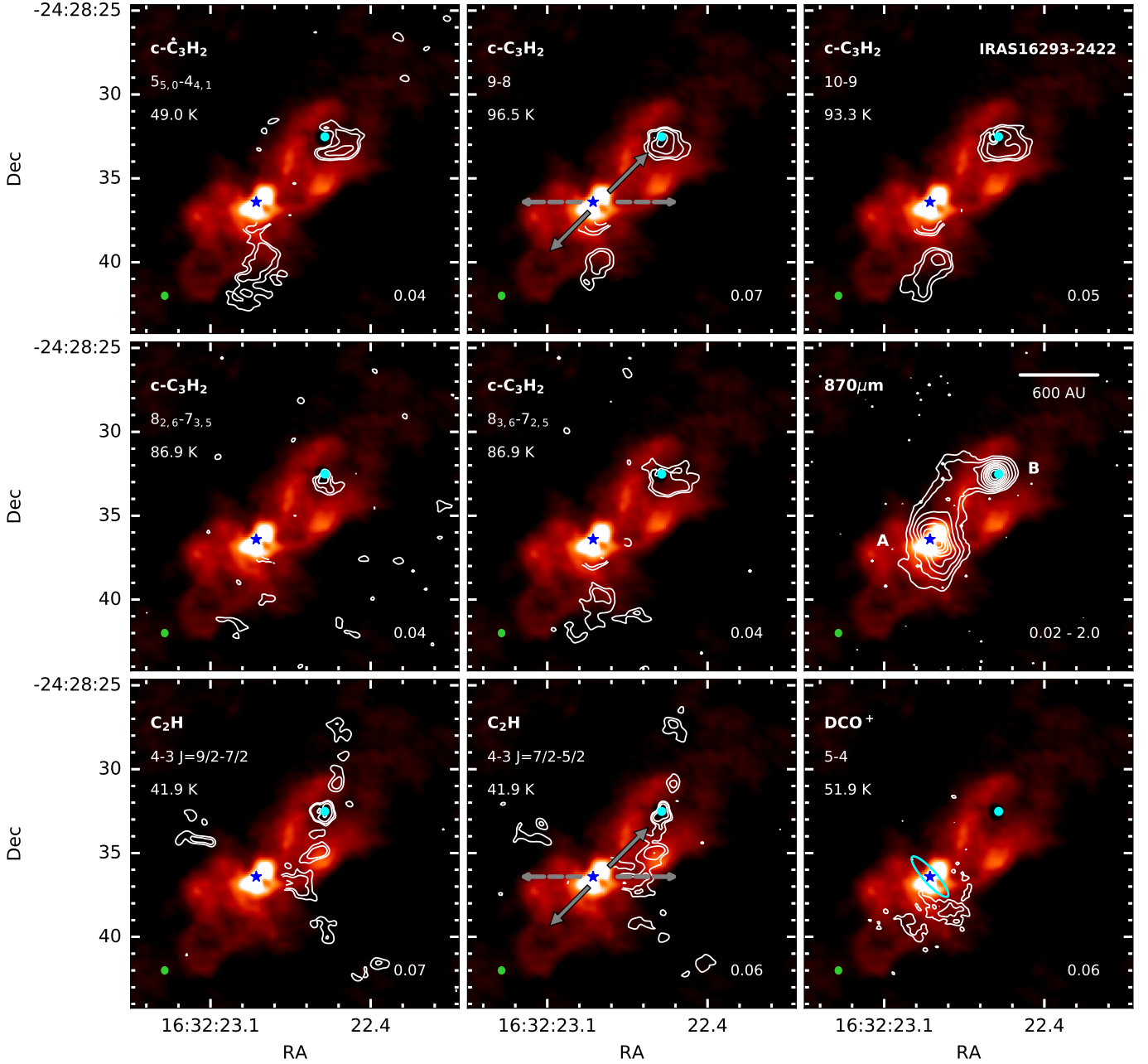


Fig. 2. Intensity integrated maps (contours) of $c\text{-C}_3\text{H}_2$, C_2H , DCO^+ , and continuum toward IRAS 16293–2422. Intensity integrated H_2CO 5–4 (0–60 km s^{-1}) is shown in color scale. Contours show the respective lines in steps of 2, 3, 5, 20, and 60σ , with σ ($\text{Jy beam}^{-1} \text{ km s}^{-1}$) indicated in the *lower right* of each panel. For continuum at $870 \mu\text{m}$, the levels are logarithmically spaced between 0.02 and 2 Jy beam^{-1} , and highlight the ridge that spans between sources A and B. The positions of IRAS 16293–2422 A and B are indicated with a star and circle, respectively. The gray arrows indicate the outflow directions, while the cyan ellipse shows the disk-like structure. The green circle on the *bottom left panel* indicates the beam of the combined 12 m and ACA observations. For the $c\text{-C}_3\text{H}_2$ and C_2H panels, the emission centered on A is contamination from other molecule(s) and is masked out in a radius of $2''$ from the position of A.

and widths of each line are listed in Table 1. Intensity integrated maps of each line overlaid on H_2CO are shown in Fig. 2. H_2CO $5_{1,5}\text{-}4_{1,4}$ from the PILES survey (van der Wiel et al., in prep.) is used as a reference for the more extended envelope and one of the outflow directions. The nominal velocities at which most species emit at sources A and B are $V_{\text{LSR}} = 3.2$ and 2.7 km s^{-1} . $c\text{-C}_3\text{H}_2$ and C_2H spectra at selected positions are presented in Figs. 3 and B.1.

In the 5–4 (PILS) and 3–2 (SMA) transitions DCO^+ is detected, with a half-crescent shape centered around source A (Figs. 2 and 4). The peak is red-shifted and located

$\sim 2''$ southwest of source A in both transitions, consistent with the red-shifted emission of the disk-like structure to the southwest (Oya et al. 2016). Weak absorption is detected toward source B in the PILS observations, which is consistent with previous studies that indicate infall motions through an inverse P-Cygni profile (Zapata et al. 2013). The DCO^+ emission south of source A is weak, peaking at 3σ in the 5–4 transition and at 5σ in the 3–2 transition. It is slightly extended to the south along the outflow, but not as far as $c\text{-C}_3\text{H}_2$. In agreement with previous observations of DCO^+ and $c\text{-C}_3\text{H}_2$ for other objects (Spezzano et al. 2016a,b), these two molecules are spatially anti-correlated.

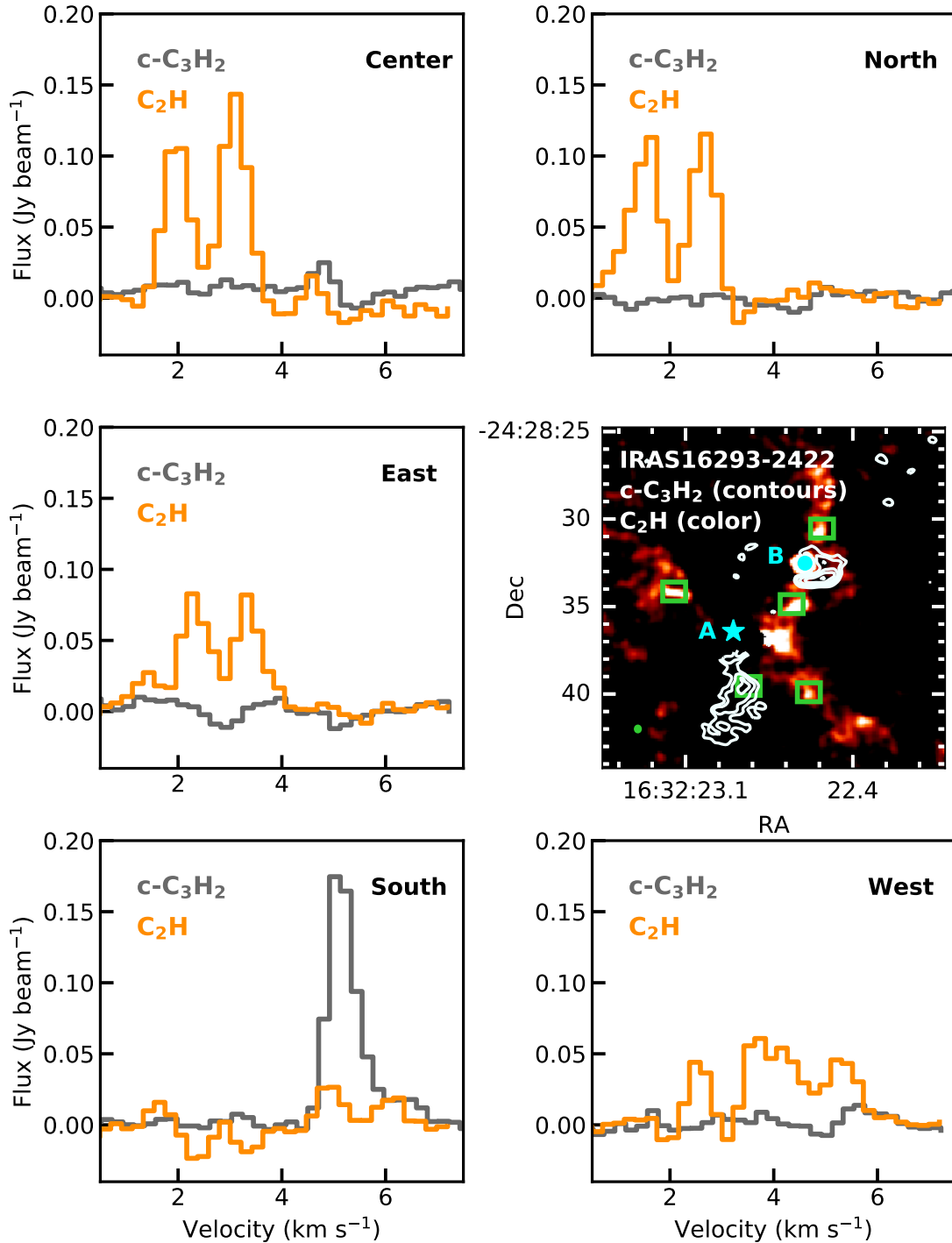


Fig. 3. IRAS 16293–2422 $c\text{-C}_3\text{H}_2$ 5–4 and C_2H 4–3 $J=9/2\text{--}7/2$ spectra taken at five positions, indicated by the green boxes in the intensity integrated map presented in the *center right panel*, while the green circle on the *bottom left panel* indicates the beam of the combined 12 m and ACA observations. The anti-correlation of both molecules is seen at all positions. The region within a radius of $2''$ from the position of source A is contaminated by other molecular species, and is masked out for these maps.

Five narrow ($FWHM \approx 1 \text{ km s}^{-1}$) lines of $c\text{-C}_3\text{H}_2$ in the 349–352 GHz frequency range with E_{up} ranging from 48 to 96 K are studied in this work. The emission peaks to the south of A, seen clearly in the top row of Fig. 2. The lines are also seen near source B, at one ALMA beam offset from the source. The southern emission extends from the circumstellar region of source A, and peaks at $\leq 5\sigma$ about $\sim 4''$ away from the source position. Toward source A itself, the spectrum is too confused to identify the separate molecular lines. Thus, the region is masked

out in the maps within $2''$ from the source position. Comparing $c\text{-C}_3\text{H}_2$ with H_2CO (Fig. 2) suggests that it could arise from one side of the southern outflow cavity wall. The asymmetric heating of the outflow cavity could be due to the behavior of the outflow from IRAS 16293 A. Observations of the outflow of IRAS 16293 A at large and small scales suggest that the outflow has shifted direction from eastwest (dashed arrow in Fig. 1) to southeast–northwest (solid arrow in Fig. 1). The shift of outflow direction could have swept up material, thus causing the

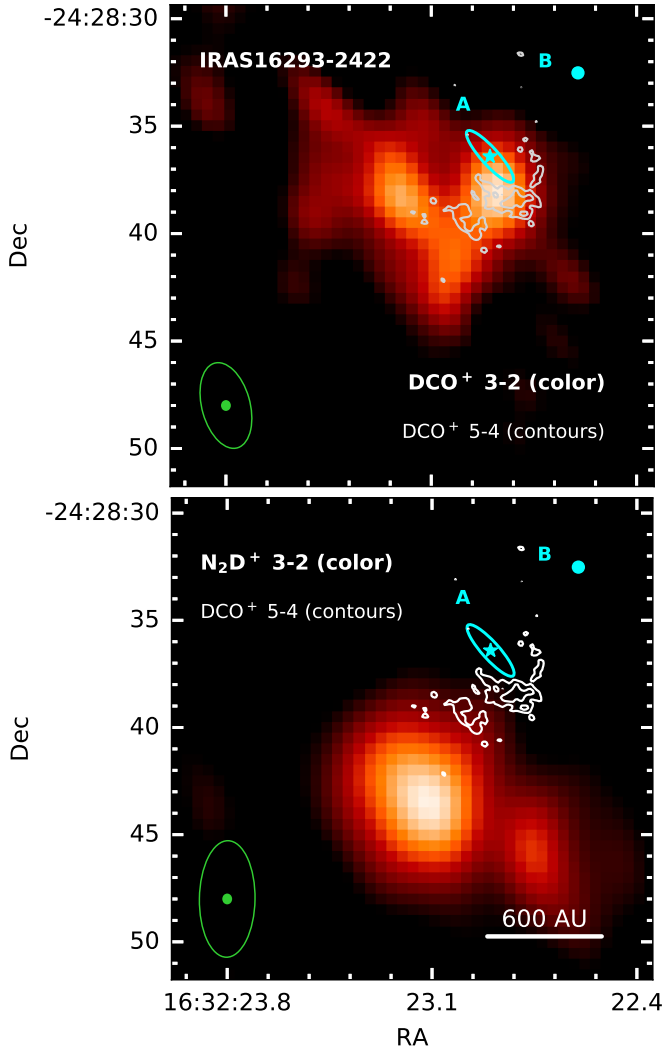


Fig. 4. Intensity integrated maps of DCO^+ 3–2 (*top panel*) and N_2D^+ 3–2 (*bottom panel*) observed with the SMA, overlaid with DCO^+ 5–4 (contours) observed with ALMA (combined 12 m array and ACA). Contours are the same as in Fig. 2 with $\sigma = 0.06 \text{ Jy beam}^{-1}$. The positions of IRAS 16293–2422 A and B are indicated with a star and circle, respectively. The cyan ellipse shows the disk-like structure. The filled green ellipses show the beam for the ALMA observations, while the unfilled ellipse shows the beam for the SMA observations. Both DCO^+ transitions match spatially, and N_2D^+ is located beyond the extent of the DCO^+ emission. We note that this figure has a different center from that of Fig. 2.

asymmetric morphology of the outflow cavity, and consequently $c\text{-C}_3\text{H}_2$ to only be present on one side of the outflow cavity. The emission around source B may either be from the circumstellar region or the outflow cavity, but due to the orientation it is difficult to say.

We clearly detect C_2H in both spin doubling transitions with each transition showing a characteristic double hyperfine structure pattern. The emission within $2''$ of source A is masked out due to contamination from other molecular species. C_2H emission is located in a filament-like structure extending from north to south, passing through source B (Fig. 2). A second, weaker structure formed by a string of clumps extends from northeast to southwest, apparently passing through source A. C_2H is diffuse and weak, peaking at $\lesssim 5\sigma$ on all off-source positions on the map (Fig. 3). The emission around source B is brighter, peaking at 10σ in the intensity integrated map. From the channel

map, the emission appears to have a subtle velocity gradient from north to south at source B. However, the C_2H emission does not match the structure and extent of $c\text{-C}_3\text{H}_2$ (or H_2CO) in either transition (Figs. 3 and B.1). It should be noted that neither C_2H nor $c\text{-C}_3\text{H}_2$ coincide with the dust ridge seen in the continuum emission (Fig. 2; see also Jacobsen et al. 2018).

The molecule N_2D^+ 3–2 is mostly resolved out in the PILS survey, but it is detected southeast of DCO^+ with the SMA (Fig. 4), located $7''$ away from the continuum position of source A with a $S/N = 7$ (Jørgensen et al. 2011). Similar to DCO^+ , there is no N_2D^+ emission toward B. No transition of N_2D^+ was covered in the Band 7 observations.

3.2. VLA 1623–2417

Two transitions of DCO^+ and one transition each of $c\text{-C}_3\text{H}_2$, N_2H^+ , and N_2D^+ were observed with ALMA in Bands 6 and 7. Additional APEX observations detected two transitions of DCO^+ and C_2H . Intensities and line widths are listed in Table 1. Figure 5 shows the intensity integrated maps for the ALMA observations. All of these molecules trace material associated with VLA 1623 A, but not the other two components of the system, VLA 1623 B and W.

The DCO^+ 3–2 ALMA 12 m array and ACA observations have been separately analyzed in detail in Murillo et al. (2015). The 3–2 ACA map shows a smooth distribution peaking southwest of the source, with the blue-shifted emission extending northeast, but no clear red-shifted counterpart southwest. Here, we present additional ALMA Band 7 12 m array observations of DCO^+ 5–4. In both transitions of DCO^+ , the red-shifted emission, located to the south of VLA 1623 A, is clearly seen and is stronger than the blue-shifted emission located to the north. The DCO^+ 5–4 emission is three times stronger than the 3–2 emission with the 12 m array, which makes the blue-shifted emission clearly visible. For both transitions, the velocity gradients are consistent. The DCO^+ 3–2 emission borders, and the disk structure observed to be driven by VLA 1623 A are relatively compact. Even more interesting, however, is that DCO^+ in the 5–4 transition extends closer to the position of VLA 1623 A than in the 3–2 transition (Fig. 5).

The molecule DCO^+ forms at temperatures below 20 K, where CO freezes out. The position of the DCO^+ 3–2 peak along the disk plane was found to be the product of disk-shadowing, which causes a temperature drop at the edge of the disk, whereas along the outflow direction no such effect was observed (Murillo et al. 2015). The APEX observations of DCO^+ in both transitions show a single peak at the systemic velocity ($3.7\text{--}4 \text{ km s}^{-1}$) and a peak intensity of 3.6 K for the 3–2 transition, the same as obtained from JCMT observations by Jørgensen et al. (2004). The beamsizes for the APEX-1 and 2 Bands covers approximately the full extent of the DCO^+ emission seen in the ACA map. For the DCO^+ 3–2 transition, the ALMA observations recover about 28% of the flux detected in the APEX observations ($117.1 \text{ Jy km s}^{-1}$ with 24 Jy K^{-1}), while 20% was recovered with the DCO^+ 5–4 ALMA observations (APEX: $53.7 \text{ Jy km s}^{-1}$ with 24 Jy K^{-1}).

One low-lying transition of $c\text{-C}_3\text{H}_2$ is detected with the short baselines of the 12 m array, but not the long baselines. The detection of $c\text{-C}_3\text{H}_2$ with only the short baselines of the 12 m array indicates that the emission is extended without a compact structure component. The $c\text{-C}_3\text{H}_2$ emission is oriented perpendicular to the disk and seems to trace the cavity of the outflow driven by VLA 1623 A out to $3''$ from the source position. There is no detection of $c\text{-C}_3\text{H}_2$ emission in the disk traced by C^{18}O or at

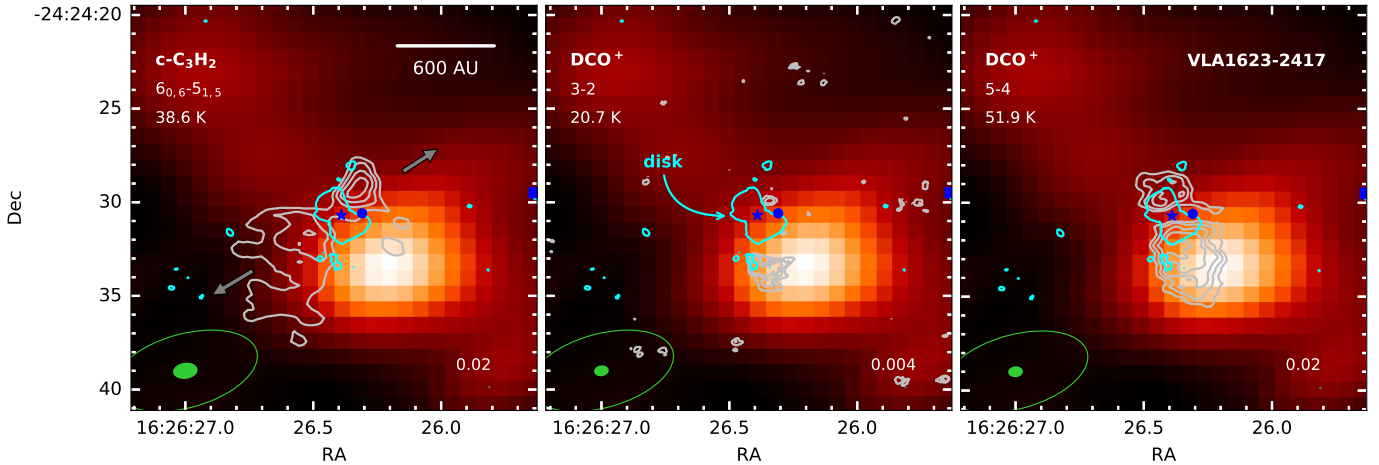


Fig. 5. Intensity integrated maps of (white contours) $c\text{-C}_3\text{H}_2$ and DCO^+ (12 m array) toward VLA 1623–2417. DCO^+ 3–2 from ACA observations is shown in color scale. The gray arrows on the *left panel* show the outflow direction. The cyan line is the 3σ contour of C^{18}O in order to show the location and extent of the rotating disk centered on VLA 1623–2417 A. Gray contours show the respective lines in steps of 3, 4, 5 and 6σ , except for DCO^+ 3–2 where the contours start at 4σ . The value of σ ($\text{Jy beam}^{-1} \text{ km s}^{-1}$) is indicated in the *lower right* of each panel. The positions of VLA 1623–2417 A, B, and W are indicated with a star, circle, and square, respectively. The filled green ellipses show the beam for the 12 m array observations (contours), while the unfilled ellipse shows the beam of the ACA observation (color scale).

the disk–envelope interface, down to the noise level. The material along the outflow cavity exhibits signatures of rotation, most notable in the southeast lobe, with a velocity range and gradient direction similar to that of DCO^+ and C^{18}O (Murillo et al. 2013). However, treating the kinematics of the outflow cavity wall traced by $c\text{-C}_3\text{H}_2$ is beyond the scope of this paper, and will be presented in a separate paper.

We detect C_2H with APEX, with the hyperfine components of each transition being clearly distinguished (Fig. 6). Both transitions are located at the systemic velocity of VLA 1623 A ($3.7\text{--}4.0 \text{ km s}^{-1}$) and show no broadening, indicating that the emission is most likely related to the envelope material of VLA 1623 A.

In our ALMA observations N_2H^+ and N_2D^+ are not detected. Possible reasons for this could be either due to the emission being very extended and thus resolved out in the interferometric observations, or the abundance of these molecules being too low to be detected. This is a surprising contrast to several other young embedded Class 0 sources which do show N_2H^+ and N_2D^+ (Jørgensen et al. 2004; Tobin et al. 2013). It is also interesting to note the lack of molecular line emission toward VLA 1623 in contrast to IRAS 16293 (Fig. 7). The nondetections of N_2H^+ and N_2D^+ are further analyzed in Sect. 4.4. H_2D^+ is also not detected in our Cycle 2 Band 7 observations, this is consistent with the JCMT observations reported by Friesen et al. (2014). H_2D^+ is not further treated in this work.

4. Analysis

DCO^+ appears to peak offset from the protostellar positions bordering the disk-like structures in both sources (Figs. 2 and 5). Here, we analyze the peak position first through chemical modeling of the observed emission (Sect. 4.1.1), and then using the line ratios to constrain the physical structure (temperature, density) and the associated chemistry (Sect. 4.1.2).

To study the physical conditions of the region traced by $c\text{-C}_3\text{H}_2$, line ratios of the detected transitions are used (Sect. 4.2). This is combined with C_2H to obtain the $c\text{-C}_3\text{H}_2/\text{C}_2\text{H}$ abundance ratio and show how the ratio varies with position (Sect. 4.3). $c\text{-C}_3\text{H}_2$ and C_2H can be produced by

the destruction of large hydrocarbons through UV irradiation (top-down chemistry), or through the accumulation of C and H atoms to form small hydrocarbons (bottom-up). Because of the many different destruction and formation pathways, chemical modeling of these two molecules is not included in this work.

4.1. DCO^+

4.1.1. DCO^+ distribution

In Murillo et al. (2015), the distribution of DCO^+ around VLA 1623 was found to be altered by the presence of a rotationally supported disk, causing the emission to shift inward along the disk plane but not along other directions. In this section, the DCO^+ emission around IRAS 16293 is modeled, aiming to find whether the distribution of DCO^+ in IRAS 16293 is product of the same phenomenon as observed in VLA 1623.

The DCO^+ chemistry is particularly sensitive to temperature. To model the observed emission for IRAS 16293 and VLA 1623, a simple steady state, analytic chemical network that accounts for the basic reactions leading to the production and destruction of DCO^+ is used.

Since CO and H_2D^+ are the precursors of DCO^+ , the production of H_2D^+ will be the rate-determining reaction in the chemical network, since it will dictate the production of DCO^+ . The H_2D^+ production and destruction reaction is given by



where the activation energy $\Delta E \sim 220 \text{ K}$ in the back reaction is due to the difference in zero-point energy. A crucial factor for deuterium chemistry is the ortho-to-para ratio of H_2 (Flower et al. 2006; Pagani et al. 2009b). This is included in the back reaction of the chemical network (Eq. (1)), since it is here where the distinction has the most significant effect (Murillo et al. 2015). The reactions and parameters for $o\text{-H}_2$ and $p\text{-H}_2$ were adapted from Walmsley et al. (2004). The ortho-to-para ratio is set to have a lower limit of 10^{-3} at low temperatures, as constrained from observations and models (Flower et al. 2006). The rate coefficient for the two-body reaction is expressed as

$$k = \alpha \left(\frac{T}{300} \right)^\beta \exp\left(-\frac{\gamma}{T}\right) \text{ cm}^3 \text{ s}^{-1}, \quad (2)$$

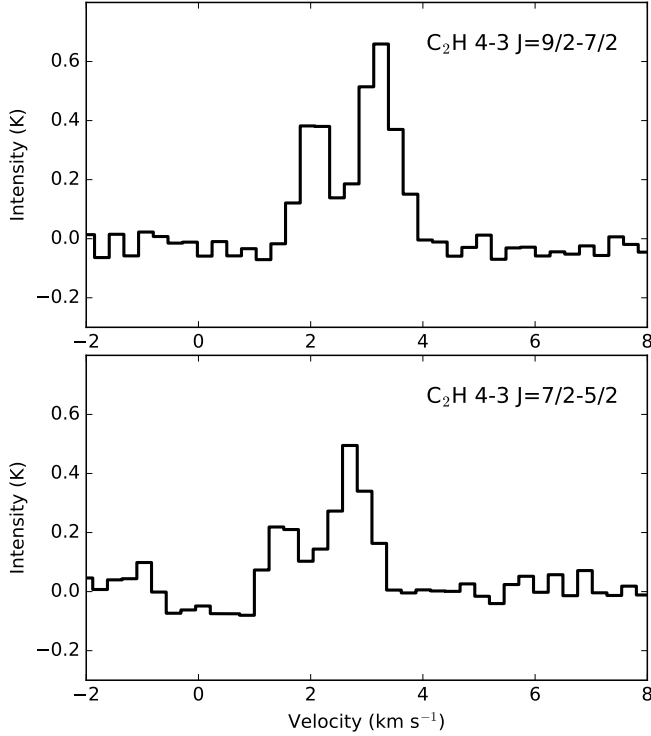


Fig. 6. Single pointing APEX observations of C_2H centered on VLA 1623–2417 A.

where T is the temperature of the gas. For cosmic ray ionization, important in the generation of H_3^+ , the rate coefficient is given by

$$k = \zeta s^{-1}, \quad (3)$$

where $\zeta = 1.26 \times 10^{-17}$ is the cosmic-ray ionization rate of H_2 . The reactions and rate coefficients used in this work are the same as those listed in Murillo et al. (2015).

Since CO is a parent molecule of DCO^+ , its abundance will impact the production of DCO^+ . The profile of the CO abundance is taken to be either constant or with a drop used to simulate freeze-out. The drop is set by the CO sublimation temperature T_{sub} and desorption density n_{de} . These limits dictate the boundary where CO is in the gas phase ($T > T_{sub}$) or freezes onto the dust grains ($T < T_{sub}$); and when the freeze-out time-scales for CO are too long ($n < n_{de}$) compared to the lifetime of the core (Jørgensen et al. 2005c). The results of the chemical modeling are passed through RATRAN (Hogerheijde & van der Tak 2000), and then synthetic data cubes are generated in order to directly compare with the observations. Because the DCO^+ emission is weak, the radial profile of the observations is obtained by using a cut with a width that covers the red-shifted peak. The model radial profile, on the other hand, is obtained from a simple cut to the synthetic data cubes since the models are symmetric flat disks. The network and further details of the model and post-processing are given in Murillo et al. (2015).

The model requires a density and temperature profile of the source as a function of radius. For IRAS 16293, the power-law density and temperature profile from Crimier et al. (2010) is adopted. Two assumptions are made, namely, the density and temperature profile is centered on IRAS 16293 A and that it is the main contributor to the luminosity of the core, consistent with the recent analysis of Jacobsen et al. (2018). Crimier

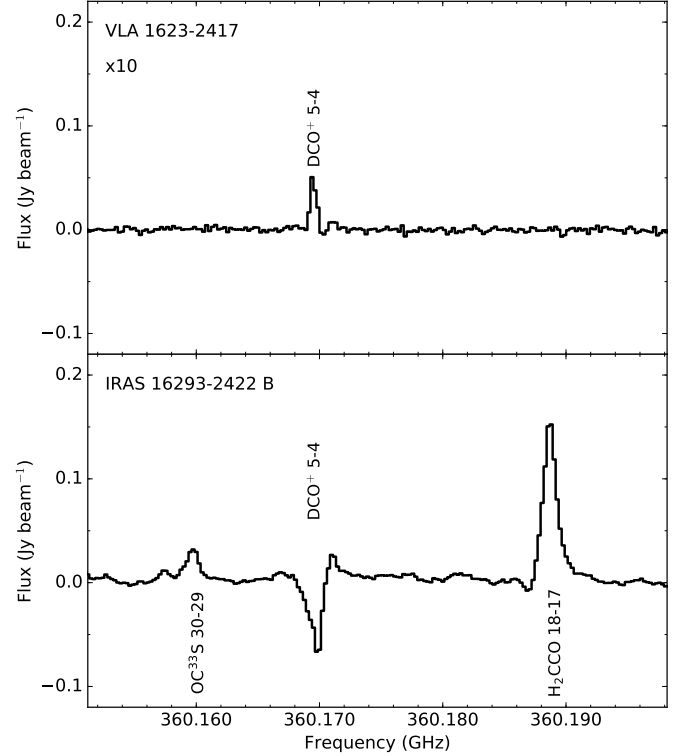


Fig. 7. Comparison of the spectra centered on DCO^+ 5–4 of VLA 1623–2417 A (12 m array) and one beam offset from IRAS 16293–2422 B (combined 12 m array and ACA). The spectra for VLA 1623–2417 has been multiplied by a factor of 10 in order to compare more easily. We note the lack of molecular line emission toward VLA 1623–2417 in contrast to IRAS 16293–2422.

et al. (2010) also showed that the emission is dominated by one of the two components, most likely IRAS 16293 A, rather than being centered between the two sources. Thus, our assumptions should not introduce major issues in our modeling. While several physical profiles have been derived for IRAS 16293 (e.g., Schöier et al. 2002), only one is adopted here since we alter the density and temperature profiles by an arbitrary factor, exploring the effects of these parameters on the production of DCO^+ . For VLA 1623, we adopt the power-law density and temperature profile from Jørgensen et al. (2002). Here again we assume the density and temperature profile is centered and dominated by VLA 1623 A. Given that VLA 1623 B does not contribute much to the line emission nor the continuum, and that VLA 1623 W is $10''$ away, this should not produce issues in the resulting model. The temperature and density profile for VLA 1623 is also altered by an arbitrary factor to study the effect on DCO^+ production. The variations in the temperature and density profiles used in this work are listed in Table 2 for both systems.

For the DCO^+ models, we explore the parameter ranges of $T_{sub} = 20\text{--}40$ K, $n_{de} = 10^5\text{--}10^8$ cm^{-3} , and $X[CO] = 10^{-7}\text{--}10^{-4}$. The parameters for the best by-eye approximation to the observed DCO^+ peak position are listed in Table 3 for both systems. The best approximated model of the DCO^+ 3–2 emission around VLA 1623 (Murillo et al. 2015) are reproduced here and compared with the results of DCO^+ toward IRAS 16293.

For both systems, we find that the constant CO abundance profile produces a DCO^+ peak further out than where it is observed (gray dashed line in fourth and fifth rows of Fig. 8), and the peak position does not shift with a change in the abundance

Table 2. Tests of the temperature and density profiles of the two sources.

Test	IRAS 16293–2422 (Crimier et al. 2010)			VLA 1623–2417 (Jørgensen et al. 2002)		
	$T_{27\text{ AU}}$ (K)	$n_{27\text{ AU}}$ (cm^{-3})	Note	$T_{4\text{ AU}}$ (K)	$n_{4\text{ AU}}$ (cm^{-3})	Note
1	300.0	2.36×10^9	unchanged	250.0	1.62×10^9	unchanged
2	300.0	2.36×10^{10}	n increased by 10	250.0	1.62×10^{10}	n increased by 10
3	300.0	2.36×10^8	n decreased by 10	250.0	1.62×10^8	n decreased by 10
4	100.0	2.36×10^9	T decreased by 3	166.7	1.62×10^9	T decreased by 1.5

Table 3. DCO⁺ best approximation model parameters.

Parameter	IRAS 16293–2422	VLA 1623–2417
T_{peak} (K)	17–19	11–16
Drop boundaries:		
T_{sub} (K)	35	35
n_{de} (cm^{-3})	$\leq 10^6$	3×10^6
CO abundance:		
Inner X_{in}	10^{-5}	10^{-5}
Drop X_{D}	10^{-6}	10^{-7}
Outer X_0	10^{-4}	10^{-4}

(Murillo et al. 2015). The drop CO abundance profile produces a peak within the drop boundaries, T_{sub} and n_{de} . Altering these parameters changes the shape but not the position of the DCO⁺ peak (see Murillo et al. 2015).

Since the chemical conditions do not alter the peak position, the physical structure is examined. The original source density and temperature profiles for both sources also do not reproduce the position of the DCO⁺ peak. Increasing or decreasing the density by one order of magnitude causes the DCO⁺ peak to either shift outward or remain at a position similar to the unchanged density profile. Interestingly, only reducing the temperature profile by an arbitrary factor together with the drop CO abundance profile, causes the DCO⁺ peak to shift inward for both systems (orange solid line in Fig. 8). A by-eye fit of the chemical model to the observations is used to constrain the decrease in the temperature profile (Fig. 8). The factor is constrained to be 1.5 ± 0.2 for VLA 1623 and 3.0 ± 0.2 for IRAS 16293. This is consistent with the results found for the DCO⁺ 3–2 toward VLA 1623 in Murillo et al. (2015), which explores the physical and chemical parameter space in more detail. Thus, the observed DCO⁺ peak position is produced by a drop in the temperature along the plane perpendicular to the outflow(s). This drop in temperature can be caused by a structure, such as a disk, which shadows the outer regions, allowing the peak emission of molecules whose abundance is enhanced in cold gas to move inward.

It should be noted, however, that our simple chemical model cannot fully explain the inner part of the DCO⁺ 5–4 emission observed toward VLA 1623 A and IRAS 16293 A (orange and black solid lines in the bottom row of Fig. 8). DCO⁺ 5–4 emission at small radii could be located in the disk where both cold and warm chemical processes can contribute to its formation (Favre et al. 2015; Huang et al. 2017; Salinas et al. 2017). For warm DCO⁺ to form, gas with temperatures up to 70 K (Favre et al. 2015) are needed. DCO⁺ 5–4 is observed further into the disk of VLA 1623 A ($L_{\text{bol}} = 1 L_{\odot}$; Murillo & Lai 2013) than in IRAS 16293 ($L_{\text{bol}} = 18 L_{\odot}$; Jacobsen et al. 2018) due to the lower

temperature of the inner disk regions. Considering the original source profile which applies to the disk region (top row, solid red line, Fig. 8), IRAS 16293 A reaches gas temperatures of 70 K at about 1'' or 120 AU, the outer part of the 200 AU disk-like structure (Oya et al. 2016). In contrast, VLA 1623 A reaches 70 K at 0.1'' or 12 AU – in other words, significantly closer to the protostar.

Thus, the distribution of the cold DCO⁺ around both VLA 1623 and IRAS 16293 is product of the presence of a disk(-like) structure, which causes a drop in temperature on the envelope gas at the edge of the disk(-like structure), that is, the disk-envelope interface. The presence of the disk(-like) structure generates an asymmetric temperature profile in the protostellar system.

4.1.2. Line ratios and implied physical conditions

Line ratios can provide an independent measure of the temperature of the region being traced by a molecule. The ratio of DCO⁺ 5–4/3–2 will provide an independent test of the results obtained with the chemical model of DCO⁺ described in the previous section.

Using RADEX (van der Tak et al. 2007), we performed non-LTE excitation and radiative transfer calculations to constrain the temperature and density of the regions being traced by comparing the ratios of observed molecular lines with those calculated by the non-LTE excitation. We limit the range of H₂ densities based on the source profile used for chemical modeling (Table 2 and Fig. 8) and the radial position of the emission being modeled. Using RADEX the column density of the emission was checked to see if it is produced by molecular line emission that is optically thin or thick at H₂ densities of $1\text{--}8 \times 10^7 \text{ cm}^{-3}$ for IRAS 16293 and $2\text{--}6 \times 10^6 \text{ cm}^{-3}$ for VLA 1623. For the best-fitting column densities of $(2\text{--}3) \times 10^{12} \text{ cm}^{-2}$ and H₂ densities of $10^6\text{--}10^8 \text{ cm}^{-3}$, the DCO⁺ 3–2 and 5–4 emission is optically thin in both sources (Table 4). To produce optically thick lines, column densities of $>7 \times 10^{12} \text{ cm}^{-2}$ would be needed for a temperature of 20 K. As the emission of both lines are optically thin, the line intensity ratios are not affected by the adopted column density. All the molecular data files used in this work are obtained from the Leiden Atomic and Molecular Database (LAMDA; Schöier et al. 2005). The collisional rate coefficients for DCO⁺ are based on the results of Botschwina et al. (1993) and Flower (1999). In order to compare the observed peak intensities with the results from RADEX, the observed peak intensities are converted from Jy beam^{−1} to K using the relation $T_{\text{mb}} = 1.36 \lambda^2 / \theta^2 I_{\nu, \text{obs}}$ where λ is the wavelength in centimeters of the molecular transition, θ is the beam of the observations and $I_{\nu, \text{obs}}$ is the observed peak intensity in mJy beam^{−1}.

Here, we derive the physical parameters from the DCO⁺ 5–4/3–2 ratio for both sources. Figure 9 shows the variation of the DCO⁺ 5–4/3–2 ratio with H₂ density and temperature. For

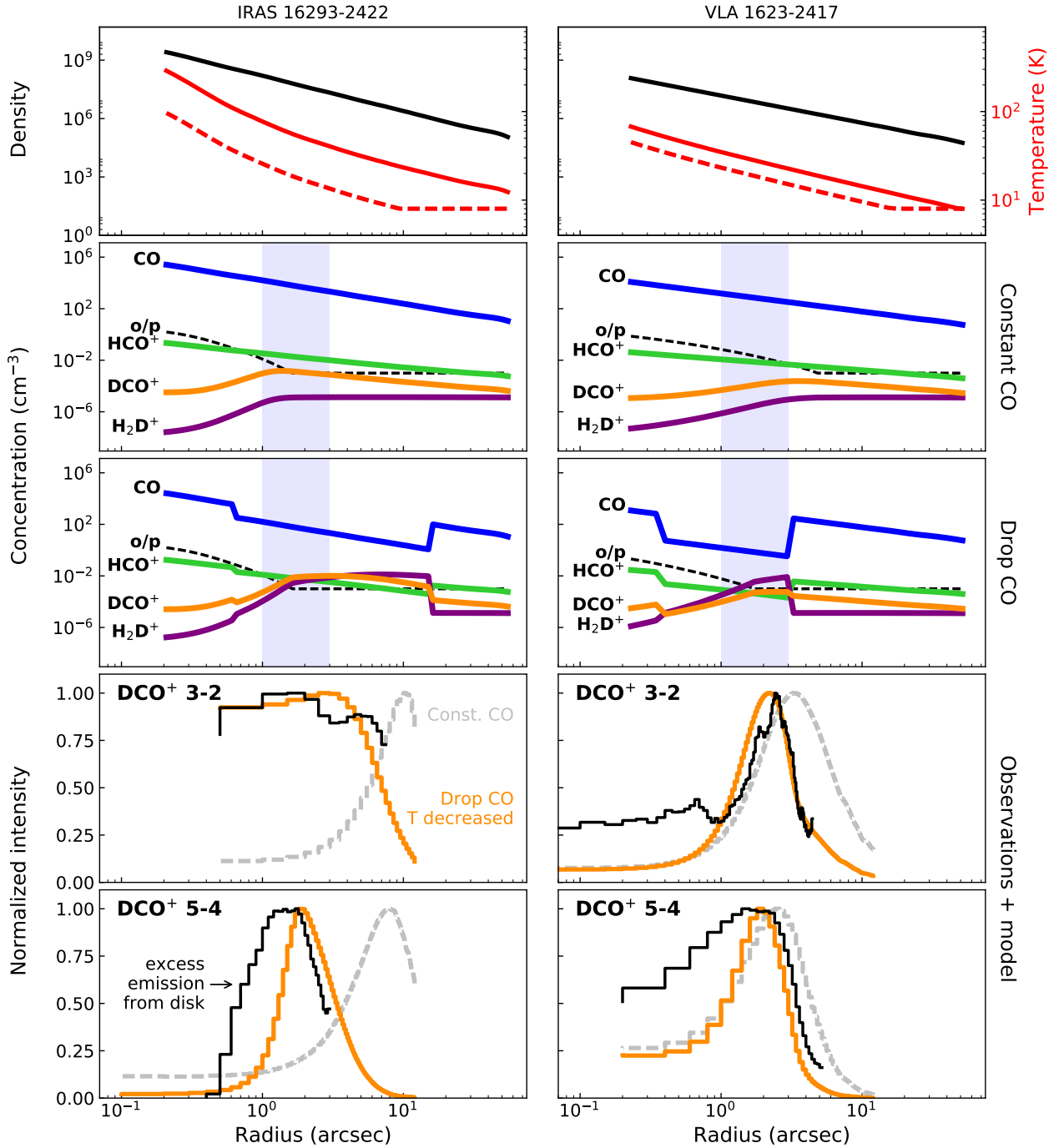


Fig. 8. Results from modeling the observed DCO^+ peak with our simple analytic chemical model. The *left column* shows results for IRAS 16293–2422, while the *right column* shows those for VLA 1623–2417. The *top row* shows the input density (black) and temperature (red) as functions of radius for each system. The solid red line shows the original temperature profile used for the constant CO model (*second row*). The dashed red line is the profile decreased by factors of 3 and 1.5 for IRAS 16293–2422 and VLA 1623–2417, respectively, and used for the drop CO model (*third row*). The lower limit on the temperature is set at 8 K. In the *second and third rows*, the shaded range is the location of the observed DCO^+ peak. The *fourth and fifth rows* show the observed radial profiles of DCO^+ (black lines) overlaid with both Constant (dashed gray lines) and Drop CO models (solid orange lines). In all panels, the protostellar source is located on the left, and the envelope on the right, with the peak position of DCO^+ indicating the disk-envelope interface. We note that the excess DCO^+ 5–4 emission from the disk(-like) regions is not well reproduced by the cold DCO^+ network.

both IRAS 16293 and VLA 1623, the red-shifted peak emission is considered, since it is the most prominent. The results for IRAS 16293 and VLA 1623 are compared in Table 4.

For IRAS 16293, a ratio DCO^+ 5–4/3–2 = 0.6 ± 0.1 is obtained from the PILS Band 7 observations and the SMA 230 GHz observations (Jørgensen et al. 2011). We note that for

IRAS 16293, we only used the peak intensity from the ACA observations, and thus pick up emission from scales similar to the SMA observations. Thus, beam dilution does not need to be taken into consideration. We adopted a line width of 1.0 km s^{-1} and a column density of $3 \times 10^{12} \text{ cm}^{-2}$, a value that also reproduces the observed line intensities. For densities

Table 4. DCO⁺ intensities and line ratios, with inferred temperature and density.

Source	IRAS 16293–2422		VLA 1623–2417 – ALMA		VLA 1623–2417 – APEX	
Transition	5–4 (ACA)	3–2 (SMA)	5–4	3–2	5–4	3–2
Line width (km s ⁻¹)	1.0	1.0	0.6	0.6	0.7	0.7
Beam (arcsec)	5.25 × 2.36	4.11 × 2.45	0.87 × 0.65	0.85 × 0.54	17.3	28.9
Peak (Jy beam ⁻¹)	3.8 ± 0.6	1.9 ± 0.2	0.29 ± 0.02	0.087 ± 0.008
Peak (K)	2.9 ± 0.4	4.9 ± 0.6	4.8 ± 0.3	4.9 ± 0.5	0.79 ± 0.1 ^a	4.8 ± 0.1
Line ratio	0.6 ± 0.1		1.0 ± 0.1		0.2 ± 0.03	
Column density (cm ⁻²)	3 × 10 ¹²		2 × 10 ¹²		2 × 10 ¹²	
H ₂ density (cm ⁻³)	1–8 × 10 ⁷		2–6 × 10 ⁶		1–6 × 10 ⁶	
Kinetic temperature (K)	20–23		30–55		12–19	
τ	<1		<1		<1	

Notes. ^(a)Peak temperature with beam dilution factor applied to DCO⁺ 5–4 (see Appendix C), taking the beam to be 17.3'', and source 28.9''.

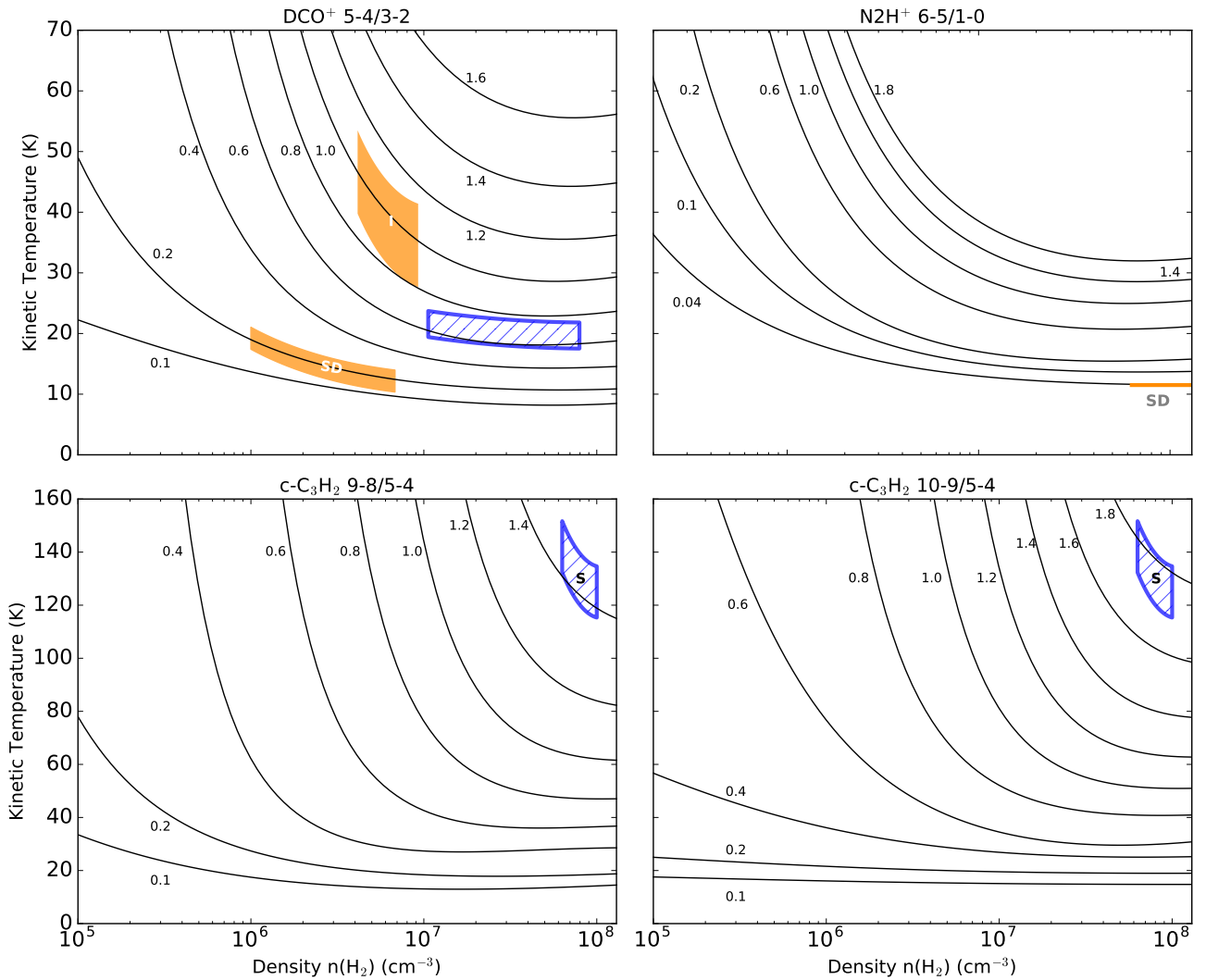


Fig. 9. Calculated line brightness temperature ratios for DCO⁺ 5–4/3–2, N₂H⁺ 6–5/1–0 and c–C₃H₂ 10–9/5–4, and 9–8/5–4. Black lines show the modeled ratios assuming column densities of 2.5×10^{12} , and 1.3×10^{13} cm⁻² for DCO⁺ and N₂H⁺, respectively, and 7×10^{13} for both c–C₃H₂ ratios. Colored regions indicate the observed line ratios drawn over the range of densities and temperatures that characterize the observed emission, for IRAS 16293–2422 with ALMA (hatched blue) and VLA 1623–2417 (solid orange) with single-dish (SD) and interferometric (I) observations. For c–C₃H₂, the value for IRAS 16293–2422 is from the south position.

below 10^6 cm⁻³, the critical density of the 5–4 transition, the line ratio is primarily sensitive to density; at higher densities, the

ratio becomes a good temperature probe. According to the density structure presented in Fig. 8 (top panel), the density at the

Table 5. $c\text{-C}_3\text{H}_2$ inferred parameters and abundance ratio for $c\text{-C}_3\text{H}_2/\text{C}_2\text{H}$.

Position	Coordinates		9–8/5–4	10–9/5–4	n_{H_2} (cm^{-3})	T_{kin} (K)	$N_{c\text{-C}_3\text{H}_2}^{a,b}$ (cm^{-2})	$N_{\text{C}_2\text{H}}^d$ (cm^{-2})	$c\text{-C}_3\text{H}_2/\text{C}_2\text{H}$
	RA	Dec							
IRAS 16293–2422									
South	16:32:22.88	–24:28:39.78	1.4 ± 0.07	1.7 ± 0.08	$5\text{--}10 \times 10^7$	120 – 155	9.3×10^{13}	$\leq 3 \times 10^{13}$	≥ 3.1
Center	16:32:22.69	–24:28:35.16			$1\text{--}6 \times 10^{7c}$	50 – 120	$5\text{--}7 \times 10^{12}$	2×10^{14}	≤ 0.035
North	16:32:22.55	–24:28:30.28			$1\text{--}6 \times 10^{7c}$	50 – 120	$5\text{--}7 \times 10^{12}$	2×10^{14}	≤ 0.035
VLA 1623–2417 $c\text{-C}_3\text{H}_2$ $6_{0,6}\text{-}5_{1,5}$									
$c\text{-C}_3\text{H}_2^d$	16:26:26.39	–24:24:30.69	$5\text{--}10 \times 10^7$	120–155	$5.3\text{--}6.7 \times 10^{10}$	3×10^{13}	0.002^e

Notes. ^(a)For IRAS 16293–2422, column densities are for a beam of $0.5''$. For VLA 1623–2417, column densities are for a beam of $17.3''$, corresponding to the beam of the C_2H observations. ^(b)An $o/p = 3$ was used to calculate the total column density of $c\text{-C}_3\text{H}_2$. ^(c)Densities are assumed from the model envelope. ^(d) $c\text{-C}_3\text{H}_2$ n_{H_2} and T_{kin} parameters taken from the south position of IRAS 16293–2422. ^(e)Due to the different scales being picked up by the observations, the ratio is not well determined, and is provided here for reference.

peak DCO^+ emission position is higher than the critical density, so a kinetic temperature between 20 and 23 K can be inferred for IRAS 16293. This temperature is consistent with the chemical modeling of the DCO^+ peak position.

For VLA 1623, the ALMA 12 m array observations provide DCO^+ $5\text{--}4/3\text{--}2 = 1.0 \pm 0.1$. The beam-size of DCO^+ $5\text{--}4$ ($0.87'' \times 0.65''$) is similar to that of the $3\text{--}2$ transition ($0.87'' \times 0.54''$) and thus no beam dilution factor was added to the calculation. This line brightness temperature ratio implies a kinetic temperature between 30 and 55 K, adopting a column density of 2×10^{12} and a line width of 0.7 km s^{-1} to reproduce the observed peak intensities. This is higher than expected from the chemical modeling of DCO^+ . The APEX observations are used to double check if this is the kinetic temperature of the bulk of the DCO^+ emission at the disk–envelope interface. The APEX DCO^+ data give a much lower line ratio, $5\text{--}4/3\text{--}2 = 0.2 \pm 0.03$. This line brightness temperature ratio is well reproduced by a kinetic temperature of 12–19 K, in agreement with the chemical model. It is likely that the ALMA 12 m array observations are picking up both warm and cold DCO^+ emission in the $5\text{--}4$ transition, but only cold DCO^+ in the $3\text{--}2$ transition. On the other hand, the APEX observations are recovering DCO^+ emission from the cold regions at the edge of the disk and the envelope, but the beam size dilutes the emission from the inner regions. This then causes the discrepancy of derived kinetic temperatures that we obtain from interferometric vs. single-dish data. The temperature from the interferometric data is driven up due to more emission being detected in the higher transition.

4.2. $c\text{-C}_3\text{H}_2$ excitation

Five transitions of $c\text{-C}_3\text{H}_2$ are detected toward IRAS 16293. Temperature is derived from the $c\text{-C}_3\text{H}_2$ 9–8/5–4 and 10–9/5–4 ratios following the same method as in Sect. 4.1. The collisional rate coefficients for $c\text{-C}_3\text{H}_2$ are based on Chandra & Kegel (2000). The density range is chosen based on the envelope model of IRAS 16293. Figure 9 shows the line brightness temperature ratios as functions of H_2 density and kinetic temperature. The ortho- $c\text{-C}_3\text{H}_2$ molecular file is used for the RADEX calculations since the $5\text{--}4$ transition (349.264 GHz) presented here is the ortho form (para- $c\text{-C}_3\text{H}_2$ $5\text{--}4$ is at 338.204 GHz). To convert to the total (ortho + para) $c\text{-C}_3\text{H}_2$ column density, an o/p ratio of 3 was used. Three regions covering the south $c\text{-C}_3\text{H}_2$ peak and the C_2H peaks near the center and north of the

map are selected to derive the temperature and $c\text{-C}_3\text{H}_2/\text{C}_2\text{H}$ column density ratios (Fig. 3). For the position with no detections of either molecule, the peak intensity from within the box used to probe the respective position (Fig. 3) is used. These values are listed in Table C.1. Table 5 lists the positions. The IRAS 16293 A and B positions are not modeled due to contamination from other molecular species.

Both $c\text{-C}_3\text{H}_2$ 9–8/5–4 and 10–9/5–4 ratios are simultaneously fit for the south position. For the center and north positions, a temperature of 50–120 K is assumed and the column density is calculated assuming an upper limit of three times the rms noise for the peak temperature brightness. Table 5 lists the derived kinetic temperature from the $c\text{-C}_3\text{H}_2$ ratio together with the assumed $c\text{-C}_3\text{H}_2$ column densities for the regions being traced. The total column density for $c\text{-C}_3\text{H}_2$ is calculated assuming an ortho-to-para ratio of 3. The peak intensities for each transition are listed in Table C.1. We find that the temperature for the south $c\text{-C}_3\text{H}_2$ peak, corresponding to the outflow cavity of IRAS 16293 A, is between 120 and 155 K. Comparing the temperatures obtained from $c\text{-C}_3\text{H}_2$ and DCO^+ line ratios, it is clear that $c\text{-C}_3\text{H}_2$ arises from a much warmer region than DCO^+ . This is linked to the spatial anti-correlation found for these two molecules, both in our observations and other work (see Sect. 5).

Only one transition of $c\text{-C}_3\text{H}_2$ is available for VLA 1623, with an upper level energy (38.6 K) lower than those observed toward IRAS 16293 ($\geq 49 \text{ K}$). Thus, to obtain an idea of the column densities in the region traced by $c\text{-C}_3\text{H}_2$ toward VLA 1623, we adopt the temperature and density from the $c\text{-C}_3\text{H}_2$ line ratios toward IRAS 16293 at the south peak. The $c\text{-C}_3\text{H}_2$ south peak of IRAS 16293 is chosen due to the fact that it traces the outflow cavity, as it does for VLA 1623. Using the parameters of $c\text{-C}_3\text{H}_2$ from the south position of IRAS 16293, the derived column density is $2 \times 10^{13} \text{ cm}^{-2}$ for a beam of $1.6'' \times 0.88''$, lower than that found for the south peak of IRAS 16293 by about a factor of 5, and similar to the column density found for the central position of the IRAS 16293 map. If the beam from the C_2H observations is considered ($17.3''$), the derived column density of $c\text{-C}_3\text{H}_2$ becomes a few 10^{10} cm^{-2} (Table 5).

4.3. $c\text{-C}_3\text{H}_2 / \text{C}_2\text{H}$ abundance ratio

The same transitions of C_2H are observed toward both sources, with ALMA for IRAS 16293 and with APEX for VLA 1623. The peak intensities are listed in Table C.1. Since C_2H ratios

are not sensitive to temperature or density given the similar upper energies E_{up} (Table 1), the method adopted for DCO^+ and $c\text{-C}_3\text{H}_2$ cannot be used here. Instead, the C_2H column density is derived by assuming the kinetic temperature and number density obtained from $c\text{-C}_3\text{H}_2$ line ratios. Using the same derived temperature and density for C_2H from $c\text{-C}_3\text{H}_2$ for the corresponding position is done to probe the parameters of C_2H if it is tracing the same region as $c\text{-C}_3\text{H}_2$. The results are listed in Table 5.

The south position in IRAS 16293 presents a column density of $\leq 3 \times 10^{13} \text{ cm}^{-2}$ for C_2H , about an order of magnitude lower compared to the center and north positions which have a column density of $2 \times 10^{14} \text{ cm}^{-2}$. Table 5 lists the $c\text{-C}_3\text{H}_2/\text{C}_2\text{H}$ column density ratio for each position. It must be noted that the ratio at the south position is a lower limit, whereas for the central and north position, it is an upper limit. The differences in ratios between positions reflect the anti-correlation of the two molecules in the IRAS 16293 system. Most certainly, the anti-correlation is not due to critical densities, since the derived number densities of $c\text{-C}_3\text{H}_2$ (10^7 to 10^8 cm^{-3}) at all points are above the critical densities of both C_2H (8×10^4 to $6 \times 10^5 \text{ cm}^{-3}$) and $c\text{-C}_3\text{H}_2$ ($2\text{--}5 \times 10^5 \text{ cm}^{-3}$).

For VLA 1623, C_2H column densities are found to be a few times 10^{13} cm^{-2} , lower than the peaks of C_2H detected toward IRAS 16293. The difference in column densities are most likely be due to beam dilution effect from the observations with APEX. Thus the $c\text{-C}_3\text{H}_2/\text{C}_2\text{H}$ ratio is not well determined for VLA1623. The results are listed in Table 5.

4.4. N_2H^+ and N_2D^+

For VLA 1623, the ALMA 12 m array observations of N_2D^+ and N_2H^+ did not detect any emission. Since these molecules are readily detected in other sources (e.g., Tobin et al. 2013), the cause of this nondetection is examined. Two cases are explored, extended and compact emission concentrated in a $1''$ region. The details of the analysis are given in Appendix C.

In the case of extended emission, the predicted N_2H^+ 4–3 peak intensity is the same as the noise level of our observations, while for the case of the emission concentrated in $1''$ region, the S/N would be about 26. In a similar manner, the predicted N_2D^+ 3–2 peak intensity is expected to have a marginal detection in our observations for the extended emission case, and a $S/N = 40$ for the compact emission case. Thus, we should have detected both molecules in our observations if they arose from a compact structure.

5. Discussion

5.1. Comparison of IRAS 16293–2422 and VLA 1623–2417

The chemical structure of both systems is compared in this section. A cartoon of their structure is given in Fig. 10.

The DCO^+ peak position in both sources is well described by a drop in the temperature profile. This drop can be explained by the presence of a disk which shadows the envelope, causing the DCO^+ emission to move inward, closer to the source along the disk plane. For VLA 1623, the ALMA DCO^+ 5–4 observations are picking up emission coming from both the cold envelope at the edge of the disk (disk–envelope interface) and the warmer parts of the disk.

The outflow cavity wall of IRAS 16293 A and VLA 1623 A is traced by $c\text{-C}_3\text{H}_2$. Due to $c\text{-C}_3\text{H}_2$ having both top-down and bottom up chemistry, it was not studied using a chemical

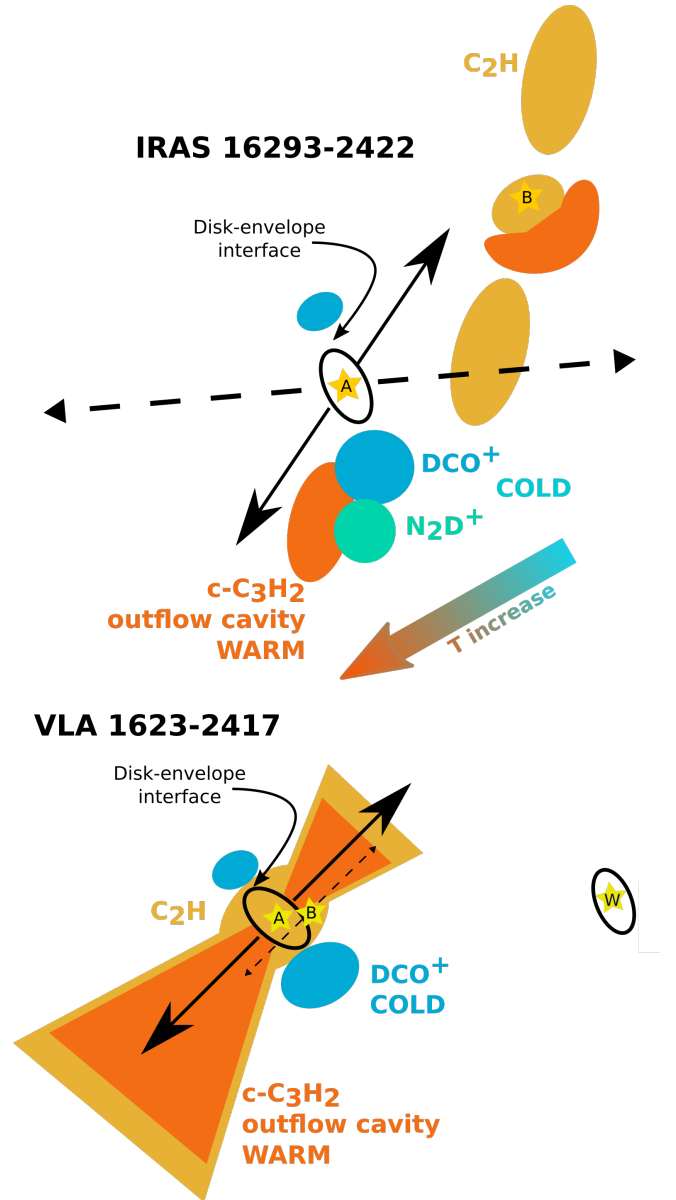


Fig. 10. Cartoon showing distribution of the molecules studied in this work toward both sources. The solid and dashed lines show outflow directions. Black ellipses indicate disk structures. C_2H toward VLA 1623–2417 A is observed with APEX, thus the distribution is expected based on the physical conditions of VLA 1623–2417, instead of direct mapping.

model. For VLA 1623 A, $c\text{-C}_3\text{H}_2$ traces the full outflow cavity (extending out to $3''$), whereas for IRAS 16293 A only one side of the south outflow cavity wall is observed. It is possible that the $c\text{-C}_3\text{H}_2$ emission is product of UV radiation from the central source, and the warmer temperatures found in the outflow cavity. UV radiation liberates atomic carbon which leads to gas-phase formation of small hydrocarbons. Chemical models of the outflow cavity walls show that $c\text{-C}_3\text{H}_2$ is initially concentrated around the outflow wall, and progressively moves to the disk plane as the cavity widens with age, irradiating more envelope material (Drozdovskaya et al. 2015). Higher temperatures could accelerate certain chemical processes in the protostellar envelope, while movement of material through outflows, rotation, and infall could bring dust with $c\text{-C}_3\text{H}_2$ precursors (e.g., CH_4 , C_2H_2) closer to areas where they can be sublimated

and thus enhance the $c\text{-C}_3\text{H}_2$ gas. Hence, the differences in the spatial distributions of $c\text{-C}_3\text{H}_2$ in IRAS 16293 A ($L_{\text{bol}} > 18 L_{\odot}$; [Jacobsen et al. 2018](#)) and VLA 1623 A ($L_{\text{bol}} \sim 1 L_{\odot}$) could be the product of age, luminosity, or core dynamics. In any case, the presence of $c\text{-C}_3\text{H}_2$ emission is due to the temperature of the region where it is observed.

The molecule C_2H does not present similar distributions in IRAS 16293 and VLA 1623. For VLA 1623, the single-dish observations of C_2H showed no emission was detected in the off positions, thus we expect that C_2H peaks around VLA 1623 A. Given the observations, low temperatures in the envelope of VLA 1623 A as well as the envelopes of VLA 1623 B and W, and the formation mechanism of the two molecules, it might be possible that C_2H is spatially correlated with $c\text{-C}_3\text{H}_2$ on $\sim 15''$ scales. However, interferometric observations are needed to verify if both molecules are correlated toward VLA 1623. On larger scales, part of the C_2H could also come from the envelope, given that it shows similar broadening with DCO^+ ([Lindberg et al. 2017](#)).

For IRAS 16293, the observed C_2H is found in the region one beam away from IRAS 16293 B, but does not show relation with the position or outflow of IRAS 16293 A, nor with the dust ridge connecting both sources. Beyond IRAS 16293 B, C_2H and $c\text{-C}_3\text{H}_2$ are not spatially correlated (Figs. 3 and B.1). This anti-correlation is unexpected from chemical models (e.g., [Gerin et al. 2011](#); [Drozdovskaya et al. 2015](#); [Guzmán et al. 2015](#)) or observations (see Sect. 5.2). The $c\text{-C}_3\text{H}_2/\text{C}_2\text{H}$ ratio is expected to be lowered with age, that is as the protostar evolves (O. Sipilä, priv. comm.). If the different distributions of $c\text{-C}_3\text{H}_2$ and C_2H are product of age, it would suggest that IRAS 16293 and VLA 1623 are young; however, lowering the ratio with age does not explain the anti-correlation observed within IRAS 16293.

A possible explanation may be top-down chemistry producing small hydrocarbons through UV destruction of large aromatic molecules as inferred for lower density PDRs ([Guzmán et al. 2015](#)), producing different amounts of the two molecules. Another possibility for the anti-correlation might be explained by the destruction of C_2H in reactions with sulfur, nitrogen, oxygen or carbon chains ([Sakai & Yamamoto 2013](#)). The full Band 7 spectrum is examined at the $c\text{-C}_3\text{H}_2$ peak position (Figs. D.1–D.3) in order to examine whether products of C_2H reactions are present. C_2S , product of C_2H reacting with sulfur ([Drozdovskaya et al. 2018](#)), is not detected. In fact, little else is observed in the dense gas south of IRAS 16293 A. Apart from $c\text{-C}_3\text{H}_2$, only H_2CS ([Drozdovskaya et al. 2018](#)) and a few common species like HCO^+ , H_2CO , and CH_3OH are detected, which is unexpected given that outflow cavity would be irradiated and encourage chemical complexity ([Drozdovskaya et al. 2015](#)). Reactions of C_2H with carbon chains C_n would cause production of C_{n+2} and hydrogen, rendering these products undetectable due to lack of dipole moments. Overall, the strong anti-correlation of these molecules remains a chemical puzzle.

We detect N_2D^+ $7''$ south of IRAS 16293 A with the SMA (Fig. 4), bordering the DCO^+ emission ([Jørgensen et al. 2011](#)). In contrast, N_2D^+ and N_2H^+ are not detected with ALMA observations toward VLA 1623. Single-dish observations show an offset of about $60''$ between the position of VLA 1623 and the peak of N_2H^+ and N_2D^+ ([Di Francesco et al. 2004](#); [André et al. 2007](#); [Liseau et al. 2015](#); [Punanova et al. 2016](#); [Favre et al. 2017](#)). Line ratios of N_2H^+ and N_2D^+ from single-dish observations were investigated in Sect. 4.4 and Appendix C, where it was found that ALMA would detect only compact emission. Given the lack of ALMA detection of both molecules, N_2D^+ and N_2H^+ trace

extended emission outside the envelope of VLA 1623 ([Liseau et al. 2015](#)).

The presence of N_2D^+ in IRAS 16293, but not in VLA 1623, could be product of temperature differences. N_2 can be frozen out onto dust grains at temperatures below 20 K ([Bisschop et al. 2006](#)), a scenario also pointed out by [Di Francesco et al. \(2004\)](#). While other nitrogen-bearing molecules such as CN, HCN, HNC, and NO can form in the gas and on grain surfaces, N_2H^+ and N_2D^+ only form in the gas phase if N_2 gas is present. This scenario is further supported by the low temperatures found for DCO^+ . For VLA 1623 A, DCO^+ has $T_{\text{kin}} = 17$ K, and the chemical modeling suggests dust temperatures between 11 and 16 K for where DCO^+ peaks. This would indicate that further out, the temperature is even lower. In addition, at densities below $\sim 10^4 \text{ cm}^{-3}$ (two orders of magnitude below what is derived from DCO^+ for VLA 1623 A), the dust and gas temperatures decouple, and without any additional external pressure, the gas temperature drops down to 10 K ([Galli et al. 2002](#); [Evans et al. 2001](#)), which could cause N_2H^+ and N_2D^+ to recombine onto the dust grains or the precursor N_2 to freeze-out. In contrast, DCO^+ south of IRAS 16293 A indicates $T_{\text{kin}} = 20\text{--}23$ K for the gas, and dust temperatures between 17 and 19 K from chemical modeling, evidencing that the envelope of IRAS 16293 A is warmer than that of VLA 1623 A ([Jacobsen et al. 2018](#)).

The molecules N_2H^+ and N_2D^+ are thought to be tracers of evolutionary stage ([Emprechtinger et al. 2009](#)), as well as of the CO snowline ([Jørgensen et al. 2004](#); [Anderl et al. 2016](#); [van't Hoff et al. 2017](#)). These assumptions break down for very cold envelopes of embedded protostars, like that of VLA 1623. Given that some starless cores do show N_2H^+ and N_2D^+ (e.g., [Crapsi et al. 2005](#); [Tobin et al. 2013](#)), including the starless cores north of VLA 1623 ([Di Francesco et al. 2004](#); [Friesen et al. 2014](#)), it cannot be said that the cold envelope itself is an indicator of evolutionary stage. It may be possible that the ridge of material north of VLA 1623, which contains the starless cores, is being heated somehow from the side, but VLA 1623 is being shielded and thus much colder ([Di Francesco et al. 2004](#); [Bergman et al. 2011](#); [Friesen et al. 2014](#)). VLA 1623 A itself is certainly heating up the disk and outflow cavity, evidenced by DCO^+ 5–4 emission on the disk and the presence of $c\text{-C}_3\text{H}_2$ and C_2H , but on much smaller scales (< 100 AU) than in IRAS 16293 because of its lower luminosity.

5.2. Comparison with starless cores and low-mass protostars

In this section, IRAS 16293 and VLA 1623 are placed in the big picture of star formation. For this reason, the two systems described in the previous section are compared with observations of starless cores, embedded low-mass protostars and disks found in the literature. In addition, the multiplicity of the systems is also taken into consideration.

The starless core L1544 exhibits $c\text{-C}_3\text{H}_2$ close to the dense cloud core center and away from cold regions traced by DCO^+ ([Spezzano et al. 2016a,b](#)). This points to an anti-correlation between the chemistry traced by DCO^+ and that by $c\text{-C}_3\text{H}_2$, which is present in both IRAS 16293 and VLA 1623. In the system NGC 1333 IRAS 4, C_2H is observed to peak on-source toward each component, including the starless core IRAS 4C, which has the strongest emission ([Koumpia et al. 2016, 2017](#)). In the young embedded object IRAS 15398, C_2H traces the red- and blue-shifted outflow cavity ([Jørgensen et al. 2013](#)). In contrast, L1527 presents both C_2H and $c\text{-C}_3\text{H}_2$ in the envelope and disk component, with enhancements at the centrifugal barrier ([Sakai et al. 2010, 2014a, 2016](#)), but no emission along the

outflow cavity. The spatial distribution of C_2H and $c-C_3H_2$ is similar in L1527, with the emission from $c-C_3H_2$ being more compact than that of C_2H . In Oph-IRS67, C_2H and $c-C_3H_2$ exist in the same region, although the spatial extent is not the same (Artur de la Villarmois et al. 2018). In the protoplanetary disk TW Hya, C_2H and $c-C_3H_2$ are found to reside in the disk, bordering the millimeter dust, with both molecules showing an identical spatial distribution (Bergin et al. 2016). The $c-C_3H_2$ and C_2H distribution toward VLA 1623 is consistent with that observed in other protostellar systems; however, for IRAS 16293 the lack of correlation between the two molecules is still a puzzle, since no other low-mass protostar or starless core reported in the literature at present presents this situation.

In NGC1333 SVS13, N_2H^+ is detected around two of the four components of the system (Chen et al. 2009). From the system, SVS13B and SVS13C are Class 0 protostars, but the first has N_2H^+ emission while the second does not. Thus, the uneven distribution of material is not related to the evolutionary stage, but instead is most likely related to the varying envelope temperature.

Several of the systems mentioned above are multiple protostars, as are IRAS 16293 and VLA 1623. The chemical structure is found to not be homogeneous among the individual components of these systems. This would suggest that the components of wide multiple protostellar systems have no effect on the chemistry of each other. For close multiple protostellar systems, the only case shown here is that of VLA 1623 A and B, which have a separation of ~ 200 AU (based on the disk radius of VLA 1623 A and a lack of disturbance of the disk by VLA 1623 B) and show different chemical structures. However, these are only two cases, and more observations of multiple protostellar systems are needed to further understand the effect of companions on chemical structure.

5.3. Comparison with diffuse clouds, PDRs, and intermediate to high-mass protostars

Looking to compare what structures are common throughout the interstellar medium, we compare the distributions found in IRAS 16293 and VLA 1623 with diffuse clouds and PDRs. Furthermore, given that IRAS 16293 is much warmer than VLA 1623, it is also compared to high-mass protostars.

Toward the Horsehead nebula PDR, DCO^+ is observed far from the irradiated edge of the region, with no emission at the edge (Guzmán et al. 2015). The spatial anti-correlation between DCO^+ and $c-C_3H_2$ or C_2H suggests a temperature effect, as found for IRAS 16293 and VLA 1623, highlighting that DCO^+ is a really good tracer of cold regions.

Close correlation in spatial distribution $c-C_3H_2$ and C_2H is shown toward a number of PDRs, including the Orion Bar (Pety et al. 2007; van der Wiel et al. 2009; Nagy et al. 2015) and the Horsehead Nebula (Cuadrado et al. 2015; Guzmán et al. 2015), with both molecular species sitting at the irradiated, and thus warmer, edge of the region. In addition, a tight correlation between $c-C_3H_2$ and C_2H in diffuse clouds has been found (Lucas & Liszt 2000; Gerin et al. 2011; Liszt et al. 2012). The column density $c-C_3H_2/C_2H$ ratios calculated toward IRAS 16293 in the center and north positions ($c-C_3H_2/C_2H \leq 0.035$) reflect the values found for diffuse clouds ($c-C_3H_2/C_2H = 0.048$; Lucas & Liszt 2000; Liszt et al. 2012) and the envelope of L1527 ($c-C_3H_2/C_2H = 0.035-0.06$; Sakai et al. 2014a).

In high-mass star-forming regions, $c-C_3H_2$ and C_2H tend to be strongly correlated, with both lines presenting similar spatial

distributions (Mookerjee et al. 2012, 2014; Pilleri et al. 2013). In contrast, toward IRAS 20343+4129, $c-C_3H_2$ and C_2H show an anti-correlation around the outflow cavity walls of IRS 1 (Fontani et al. 2012) but not around the UC HII-region of IRS 3. The anti-correlation is explained to possibly be product of the gas density, with an enhancement of C_2H located in the regions with denser gas. Thus, the warmer envelope of IRAS 16293 does not provide a solution to the puzzle of why $c-C_3H_2$ and C_2H are anti-correlated in this system, but the difference in density, possibly caused by the outflow direction shift, might provide a possible explanation for the anti-correlation of the two molecules. Chemical processes could also be playing a role in the anti-correlation of $c-C_3H_2$ and C_2H toward IRAS 16293.

6. Conclusions

In this work, we present ALMA, SMA, and APEX observations of DCO^+ , $c-C_3H_2$, C_2H , N_2H^+ , and N_2D^+ toward IRAS 16293–2422 and VLA 1623–2417, both multiple protostellar systems in ρ Ophiuchus. The spatial distribution of each molecule is compared for both systems. DCO^+ is studied using a simple analytic chemical network coupled with radiative transfer modeling, detailed in Murillo et al. (2015), in order to determine the conditions leading to the observed peak position. Non-LTE molecular excitation and radiative transfer modeling of the observed line brightness temperature ratios is done to derive physical parameters of the regions being traced by the molecules. Finally, the observations and results of VLA 1623–2417 and IRAS 16293–2422 are compared, both between the two sources and other objects, ranging from low- to high-mass protostars, diffuse clouds and PDRs, in order to understand what structures are common.

From this work, we extract the following key points:

1. Temperature is a controlling factor of the chemical structure of a protostellar system. Disks can alter the temperature of the envelope, while UV heating can encourage the start of chemical processes in the outflow cavity.
2. An asymmetric DCO^+ structure is a good tell-tale sign for the presence of a disk, since a disk shadows the envelope at its edge, lowering the temperature and causing DCO^+ to move inward only along the disk plane.
3. $c-C_3H_2$ traces the outflow cavity of IRAS 16293–2422 and VLA 1623–2417, but shows no disk component for either source.
4. Despite both VLA 1623–2417 and IRAS 16293–2422 being low-mass Class 0 embedded objects, their structure and chemical richness varies considerably, with VLA 1623–2417 being line poor. Its much lower luminosity, and consequently lower temperatures, coupled with a large cold disk, are likely to be at the root of this difference.

Although only two sources have been studied in this work and some results in the literature, there is evidence pointing to a lack of correlation between multiplicity and the chemical structure of the envelope of these systems, at least in the embedded phase. Nevertheless, multiple systems do provide an interesting way to compare the structure with similar conditions. It would be possible, however, that the heating from companion sources would affect the chemistry as the envelope clears. Further comparison of embedded multiple protostellar systems is needed to confirm these results.

Acknowledgements. The authors thank O. Sipilä, P. Caselli, S. Spezzano, N. Sakai, C. Favre, and N. Ligterink for helpful discussions on chemistry. This paper made use of the following ALMA data: ADS/JAO.ALMA 2011.0.00902.S,

2013.1.01004.S, and 2013.1.00278.S. ALMA is a partnership of ESO (representing its member states), NSF (USA), and NINS (Japan), together with NRC (Canada) and NSC and ASIAA (Taiwan), in cooperation with the Republic of Chile. The Joint ALMA Observatory, is operated by ESO, AUI/NRAO, and NAOJ. This publication is partially based on data acquired with the Atacama Pathfinder Experiment (APEX). APEX is a collaboration between the Max-Planck-Institut für Radioastronomie, the European Southern Observatory, and the Onsala Space Observatory. We are grateful to the APEX staff for support with the observations of VLA 1623–2417. Astrochemistry in Leiden is supported by the European Union A-ERC grant 291141 CHEMPLAN, by the Netherlands Research School for Astronomy (NOVA), by a Royal Netherlands Academy of Arts and Sciences (KNAW) professor prize. The group of J.K.J. acknowledges support from the European Research Council (ERC) under the European Union's Horizon 2020 research and innovation programme (grant agreement No 646908) through ERC Consolidator Grant "S4F". Research at Centre for Star and Planet Formation is funded by the Danish National Research Foundation. M.N.D. acknowledges the financial support of the Center for Space and Habitability (CSH) Fellowship and the IAU Gruber Foundation Fellowship.

References

- Aikawa, Y., & Herbst, E. 1999, *A&A*, **351**, 233
- Aikawa, Y., Umebayashi, T., Nakano, T., & Miyama, S. M. 1999, *ApJ*, **519**, 705
- Aikawa, Y., Wakelam, V., Hersant, F., Garrod, R. T., & Herbst, E. 2012, *ApJ*, **760**, 40
- Anderl, S., Maret, S., Cabrit, S., et al. 2016, *A&A*, **591**, A3
- André, P., Martin-Pintado, J., Despois, D., & Montmerle, T. 1990, *A&A*, **236**, 180
- André, P., Belloche, A., Motte, F., & Peretto, N. 2007, *A&A*, **472**, 519
- Artur de la Villarmois, E., Kristensen, L. E., Jørgensen, J. K., et al. 2018, *A&A*, **614**, A26
- Bacmann, A., Taquet, V., Faure, A., Kahane, C., & Ceccarelli, C. 2012, *A&A*, **541**, L12
- Belitsky, V., Lapkin, I., Monje, R., et al. 2006, in *Proc. SPIE, SPIE Conf. Ser.*, **6275**, 62750G
- Bergin, E. A., Du, F., Cleeves, L. I., et al. 2016, *ApJ*, **831**, 101
- Bergman, P., Parise, B., Liseau, R., & Larsson, B. 2011, *A&A*, **527**, A39
- Bergner, J. B., Öberg, K. I., Garrod, R. T., & Graninger, D. M. 2017, *ApJ*, **841**, 120
- Bisschop, S. E., Fraser, H. J., Öberg, K. I., van Dishoeck, E. F., & Schlemmer, S. 2006, *A&A*, **449**, 1297
- Bisschop, S. E., Jørgensen, J. K., Bourke, T. L., Bottinelli, S., & van Dishoeck, E. F. 2008, *A&A*, **488**, 959
- Bogey, M., Demuyck, C., & Destombes, J. L. 1986, *Chem. Phys. Lett.*, **125**, 383
- Bogey, M., Demuyck, C., Destombes, J. L., & Dubus, H. 1987, *J. Mol. Spectrosc.*, **122**, 313
- Botschwina, P., Horn, M., Flugge, J., & Seeger, S. 1993, *J. Chem. Soc. Faraday Trans.*, **89**, 2219
- Bottinelli, S., Ceccarelli, C., Neri, R., et al. 2004, *ApJ*, **617**, L69
- Caratti o Garatti, A., Giannini, T., Nisini, B., & Lorenzetti, D. 2006, *A&A*, **449**, 1077
- Caselli, P., & Ceccarelli, C. 2012, *A&ARv*, **20**, 56
- Caselli, P., & Dore, L. 2005, *A&A*, **433**, 1145
- Cazzoli, G., Cludi, L., Buffa, G., & Pizzarrini, C. 2012, *ApJS*, **203**, 11
- Chandra, S., & Kegel, W. H. 2000, *A&AS*, **142**, 113
- Chen, X., Launhardt, R., & Henning, T. 2009, *ApJ*, **691**, 1729
- Codella, C., Cabrit, S., Gueth, F., et al. 2014, *A&A*, **568**, L5
- Coutens, A., Jørgensen, J. K., van der Wiel, M. H. D., et al. 2016, *A&A*, **590**, L6
- Crapsi, A., Caselli, P., Walmsley, C. M., et al. 2005, *ApJ*, **619**, 379
- Crimier, N., Ceccarelli, C., Maret, S., et al. 2010, *A&A*, **519**, A65
- Cuadrado, S., Goicoechea, J. R., Pilleri, P., et al. 2015, *A&A*, **575**, A82
- Di Francesco, J., André, P., & Myers, P. C. 2004, *ApJ*, **617**, 425
- Drozdovskaya, M. N., Walsh, C., Visser, R., Harsono, D., & van Dishoeck E. F. 2014, *MNRAS*, **445**, 913
- Drozdovskaya, M. N., Walsh, C., Visser, R., Harsono, D., & van Dishoeck E. F. 2015, *MNRAS*, **451**, 3836
- Drozdovskaya, M. N., van Dishoeck, E. F., Jørgensen, J. K., et al. 2018, *MNRAS*, **476**, 4949
- Dunham, M. M., Stutz, A. M., Allen, L. E., et al. 2014, *Protostars and Planets VI* (Tucson: University of Arizona Press), 195
- Dzib, S. A., Ortiz-León, G. N., Hernández-Gómez, A., et al. 2018, *A&A*, **614**, A20
- Emprechtinger, M., Caselli, P., Volgenau, N. H., Stutzki, J., & Wiedner, M. C. 2009, *A&A*, **493**, 89
- Endres, C. P., Schlemmer, S., Schilke, P., Stutzki, J., & Müller, H. S. P. 2016, *J. Mol. Spectr.*, **327**, 95
- Evans, II, N. J. 1999, *ARA&A*, **37**, 311
- Evans, II, N. J., Rawlings, J. M. C., Shirley, Y. L., & Mundy, L. G. 2001, *ApJ*, **557**, 193
- Favre, C., Bergin, E. A., Cleeves, L. I., et al. 2015, *ApJ*, **802**, L23
- Favre, C., López-Sepulcre, A., Ceccarelli, C., et al. 2017, *A&A*, **608**, A82
- Fayolle, E. C., Öberg, K. I., Garrod, R. T., van Dishoeck, E. F., & Bisschop, S. E. 2015, *A&A*, **576**, A45
- Flower, D. R. 1999, *MNRAS*, **305**, 651
- Flower, D. R., Pineau Des Forêts, G., & Walmsley, C. M. 2006, *A&A*, **449**, 621
- Fontani, F., Palau, A., Busquet, G., et al. 2012, *MNRAS*, **423**, 1691
- Friesen, R. K., Di Francesco, J., Bourke, T. L., et al. 2014, *ApJ*, **797**, 27
- Furuya, K., Aikawa, Y., Tomida, K., et al. 2012, *ApJ*, **758**, 86
- Galli, D., Walmsley, M., & Gonçalves J. 2002, *A&A*, **394**, 275
- Garay, G., Mardones, D., Rodríguez, L. F., Caselli, P., & Bourke, T. L. 2002, *ApJ*, **567**, 980
- Garrod, R. T., & Herbst, E. 2006, *A&A*, **457**, 927
- Gerin, M., Kaźmierczak, M., Jastrzebska, M., et al. 2011, *A&A*, **525**, A116
- Girart, J. M., Estalella, R., Palau, A., Torrelles, J. M., & Rao, R. 2014, *ApJ*, **780**, L11
- Güsten, R., Nyman, L. Å., Schilke, P., et al. 2006, *A&A*, **454**, L13
- Guzmán, V. V., Pety, J., Goicoechea, J. R., et al. 2015, *ApJ*, **800**, L33
- Harsono, D., Jørgensen, J. K., van Dishoeck, E. F., et al. 2014, *A&A*, **562**, A77
- Herbst, E., & van Dishoeck E. F. 2009, *ARA&A*, **47**, 427
- Hincelin, U., Wakelam, V., Commerçon, B., Hersant, F., & Guilloteau, S. 2013, *ApJ*, **775**, 44
- Hincelin, U., Commerçon, B., Wakelam, V., et al. 2016, *ApJ*, **822**, 12
- Ho, P. T. P., Moran, J. M., & Lo, K. Y. 2004, *ApJ*, **616**, L1
- Hogerheijde, M. R., & van der Tak, F. F. S. 2000, *A&A*, **362**, 697
- Huang, J., Öberg, K. I., Qi, C., et al. 2017, *ApJ*, **835**, 231
- Jacobsen, S. K., Jørgensen, J. K., van der Wiel, M. H. D., et al. 2018, *A&A*, **612**, A72
- Jørgensen, J. K., Schöier, F. L., & van Dishoeck E. F. 2002, *A&A*, **389**, 908
- Jørgensen, J. K., Schöier, F. L., & van Dishoeck E. F. 2004, *A&A*, **416**, 603
- Jørgensen, J. K., Bourke, T. L., Myers, P. C., et al. 2005a, *ApJ*, **632**, 973
- Jørgensen, J. K., Schöier, F. L., & van Dishoeck E. F. 2005b, *A&A*, **437**, 501
- Jørgensen, J. K., Schöier, F. L., & van Dishoeck E. F. 2005c, *A&A*, **435**, 177
- Jørgensen, J. K., Bourke, T. L., Nguyen Luong, Q., & Takakuwa, S. 2011, *A&A*, **534**, A100
- Jørgensen, J. K., Visser, R., Sakai, N., et al. 2013, *ApJ*, **779**, L22
- Jørgensen, J. K., van der Wiel, M. H. D., Coutens, A., et al. 2016, *A&A*, **595**, A117
- Koumpia, E., van der Tak, F. F. S., Kwon, W., et al. 2016, *A&A*, **595**, A51
- Koumpia, E., Semenov, D. A., van der Tak, F. F. S., Boogert, A. C. A., & Caux, E. 2017, *A&A*, **603**, A88
- Kristensen, L. E., Klaassen, P. D., Mottram, J. C., Schmalzl, M., & Hogerheijde, M. R. 2013, *A&A*, **549**, L6
- Li, Z.-Y., Banerjee, R., Pudritz, R. E., et al. 2014, *Protostars and Planets VI* (Tucson: University of Arizona Press), 173
- Lindberg, J. E., Jørgensen, J. K., Brinch, C., et al. 2014a, *A&A*, **566**, A74
- Lindberg, J. E., Jørgensen, J. K., Green, J. D., et al. 2014b, *A&A*, **565**, A29
- Lindberg, J. E., Charnley, S. B., & Cordiner, M. A. 2016, *ApJ*, **833**, L14
- Lindberg, J. E., Charnley, S. B., Jørgensen, J. K., Cordiner, M. A., & Bjerkeli, P. 2017, *ApJ*, **835**, 3
- Liseau, R., Larsson, B., Brandeker, A., et al. 2003, *A&A*, **402**, L73
- Liseau, R., Larsson, B., Lunttila, T., et al. 2015, *A&A*, **578**, A131
- Liszt, H., Sonnentrucker, P., Cordiner, M., & Gerin, M. 2012, *ApJ*, **753**, L28
- Loinard, L., Torres, R. M., Mioduszewski, A. J., & Rodríguez, L. F. 2008, *ApJ*, **675**, L29
- Loinard, L., Zapata, L. A., Rodríguez, L. F., et al. 2013, *MNRAS*, **430**, L10
- Lucas, R., & Liszt, H. S. 2000, *A&A*, **358**, 1069
- Lykke, J. M., Coutens, A., Jørgensen, J. K., et al. 2017, *A&A*, **597**, A53
- Maret, S., Bergin, E. A., & Lada, C. J. 2006, *Nature*, **442**, 425
- Mookerjee, B., Hassel, G. E., Gerin, M., et al. 2012, *A&A*, **546**, A75
- Mookerjee, B., Vastel, C., Hassel, G. E., et al. 2014, *A&A*, **566**, A61
- Müller, H. S. P., Klaus, T., & Winnewisser, G. 2000, *A&A*, **357**, L65
- Murillo, N. M., & Lai, S.-P. 2013, *ApJ*, **764**, L15
- Murillo, N. M., Lai, S.-P., Bruderer, S., Harsono, D., & van Dishoeck E. F. 2013, *A&A*, **560**, A103
- Murillo, N. M., Bruderer, S., van Dishoeck, E. F., et al. 2015, *A&A*, **579**, A114
- Murillo, N. M., van Dishoeck, E. F., Tobin, J. J., & Fedele, D. 2016, *A&A*, **592**, A56
- Nagy, Z., Ossenkopf, V., Van der Tak, F. F. S., et al. 2015, *A&A*, **578**, A124
- Öberg, K. I., Lauck, T., & Graninger, D. 2014, *ApJ*, **788**, 68
- Ortiz-León, G. N., Loinard, L., Kounkel, M. A., et al. 2017, *ApJ*, **834**, 141
- Oya, Y., Sakai, N., López-Sepulcre, A., et al. 2016, *ApJ*, **824**, 88
- Padovani, M., Walmsley, C. M., Tafalla, M., Galli, D., & Müller, H. S. P. 2009, *A&A*, **505**, 1199

- Pagani, L., Daniel, F., & Dubernet, M.-L. 2009a, *A&A*, 494, 719
- Pagani, L., Vastel, C., Hugo, E., et al. 2009b, *A&A*, 494, 623
- Persson, M. V., Harsono, D., Tobin, J. J., et al. 2016, *A&A*, 590, A33
- Pety, J., Goicoechea, J. R., Hily-Blant, P., Gerin, M., & Teyssier, D. 2007, *A&A*, 464, L41
- Pilleri, P., Treviño-Morales, S., Fuente, A., et al. 2013, *A&A*, 554, A87
- Pineda, J. E., Maury, A. J., Fuller, G. A., et al. 2012, *A&A*, 544, L7
- Punanova, A., Caselli, P., Pon, A., Belloche, A., & André, P. 2016, *A&A*, 587, A118
- Reipurth, B., Clarke, C. J., Boss, A. P., et al. 2014, *Protostars and Planets VI* (Tucson: University of Arizona Press), 267
- Sakai, N., & Yamamoto, S. 2013, *Chem. Rev.*, 113, 8981
- Sakai, N., Sakai, T., Hirota, T., & Yamamoto, S. 2010, *ApJ*, 722, 1633
- Sakai, N., Oya, Y., Sakai, T., et al. 2014a, *ApJ*, 791, L38
- Sakai, N., Sakai, T., Hirota, T., et al. 2014b, *Nature*, 507, 78
- Sakai, N., Oya, Y., López-Sepulcre, A., et al. 2016, *ApJ*, 820, L34
- Salinas, V. N., Hogerheijde, M. R., Mathews, G. S., et al. 2017, *A&A*, 606, A125
- Santangelo, G., Murillo, N. M., Nisini, B., et al. 2015, *A&A*, 581, A91
- Sastry, K. V. L. N., Helminger, P., Charo, A., Herbst, E., & De Lucia F. C. 1981, *ApJ*, 251, L119
- Schöier, F. L., Jørgensen, J. K., van Dishoeck, E. F., & Blake, G. A. 2002, *A&A*, 390, 1001
- Schöier, F. L., van der Tak, F. F. S., van Dishoeck, E. F., & Black, J. H. 2005, *A&A*, 432, 369
- Shirley, Y. L. 2015, *PASP*, 127, 299
- Spezzano, S., Tamassia, F., Thorwirth, S., et al. 2012, *ApJS*, 200, 1
- Spezzano, S., Bizzocchi, L., Caselli, P., Harju, J., & Brünken, S. 2016a, *A&A*, 592, L11
- Spezzano, S., Gupta, H., Brünken, S., et al. 2016b, *A&A*, 586, A110
- Stark, R., Sandell, G., Beck, S. C., et al. 2004, *ApJ*, 608, 341
- Tassis, K., Willacy, K., Yorke, H. W., & Turner, N. J. 2012, *ApJ*, 753, 29
- Tobin, J. J., Hartmann, L., Chiang, H.-F., et al. 2012, *Nature*, 492, 83
- Tobin, J. J., Bergin, E. A., Hartmann, L., et al. 2013, *ApJ*, 765, 18
- van der Tak, F. F. S., Black, J. H., Schöier, F. L., Jansen, D. J., & van Dishoeck E. F. 2007, *A&A*, 468, 627
- van der Wiel, M. H. D., van der Tak, F. F. S., Ossenkopf, V., et al. 2009, *A&A*, 498, 161
- van Dishoeck, E. F., Jansen, D. J., & Phillips, T. G. 1993, *A&A*, 279, 541
- van Dishoeck, E. F., Blake, G. A., Jansen, D. J., & Groesbeck, T. D. 1995, *ApJ*, 447, 760
- van't Hoff, M. L. R., Walsh, C., Kama, M., Facchini, S., & van Dishoeck E. F. 2017, *A&A*, 599, A101
- Vassilev, V., Meledin, D., Lapkin, I., et al. 2008, *A&A*, 490, 1157
- Visser, R., van Dishoeck, E. F., Doty, S. D., & Dullemond, C. P. 2009, *A&A*, 495, 881
- Visser, R., Doty, S. D., & van Dishoeck E. F. 2011, *A&A*, 534, A132
- Walmsley, C. M., Flower, D. R., & Pineau des Forêts, G. 2004, *A&A*, 418, 1035
- Willacy, K., Alexander, C., Ali-Dib, M., et al. 2015, *Space Sci. Rev.*, 197, 151
- Wootten, A., Andre, P., Despois, D., & Sargent, A. 1994, in *Clouds, Cores, and Low Mass Stars*, eds. D. P. Clemens, & R. Barvainis, *ASP Conf. Ser.*, 65, 294
- Yeh, S. C. C., Hirano, N., Bourke, T. L., et al. 2008, *ApJ*, 675, 454
- Yen, H.-W., Koch, P. M., Takakuwa, S., et al. 2017, *ApJ*, 834, 178
- Yoneda, H., Tsukamoto, Y., Furuya, K., & Aikawa, Y. 2016, *ApJ*, 833, 105
- Zapata, L. A., Loinard, L., Rodríguez, L. F., et al. 2013, *ApJ*, 764, L14

Appendix A: Interferometric observations**Table A.1.** Interferometric observations.

Dataset	Frequency (GHz)	UV-baseline range (k λ)	Beam (")	Largest scale (")	Field of view (")	Noise (mJy beam ⁻¹)
IRAS 16293–2422						
Combined 12 m + ACA	329.1–362.8	10 ~ 352	0.5 × 0.5	13	19.5	7–10
ACA	329.1–362.8	10 ~ 60	5.25 × 2.36	13	60	440
SMA Compact	215.6–227.6	6 ~ 91	5.5 × 3.2	20	64	240
VLA 1623–2217						
Cycle 0 12 m	216.4–232.2	25 ~ 310	0.85 × 0.56	2.5	28	4–8
Cycle 2 Band 6 12 m C35-5	215.5–221.4	18 ~ 791	0.45 × 0.25	1.9	28	7–9
Cycle 2 Band 6 12 m C34-1	215.5–221.4	11 ~ 253	1.6 × 0.88	5.3	28	20
Cycle 2 Band 7 12 m	359.0–372.7	18 ~ 420	0.87 × 0.54	3.1	17.2	26–95

Table A.1 lists details of the interferometric observations used in this work for both systems, IRAS 16293 and VLA 1623. For VLA 1623, the Cycle 2 Band 6 12 m array observations have both long (C35-5) and short (C34-1) baselines. The short baselines were observed to bridge the baseline ranges between the ACA and 12 m observations. The c-C₃H₂ observations toward VLA 1623 presented in this work were detected with the 12 m array short baselines but not the long baselines, suggesting that the emission arises from regions larger than ~0.5".

Appendix B: Additional c-C₃H₂ and C₂H spectra

The spectra for all transitions of c-C₃H₂ and C₂H toward the south, center, and north positions of IRAS 16293 are shown in Fig. B.1. The systemic velocity of IRAS 16293 A and B are marked on the spectra with dashed lines. The anti-correlation of the two molecules is evident from the spectra, as well as a slight velocity shift in C₂H between the center and north positions.

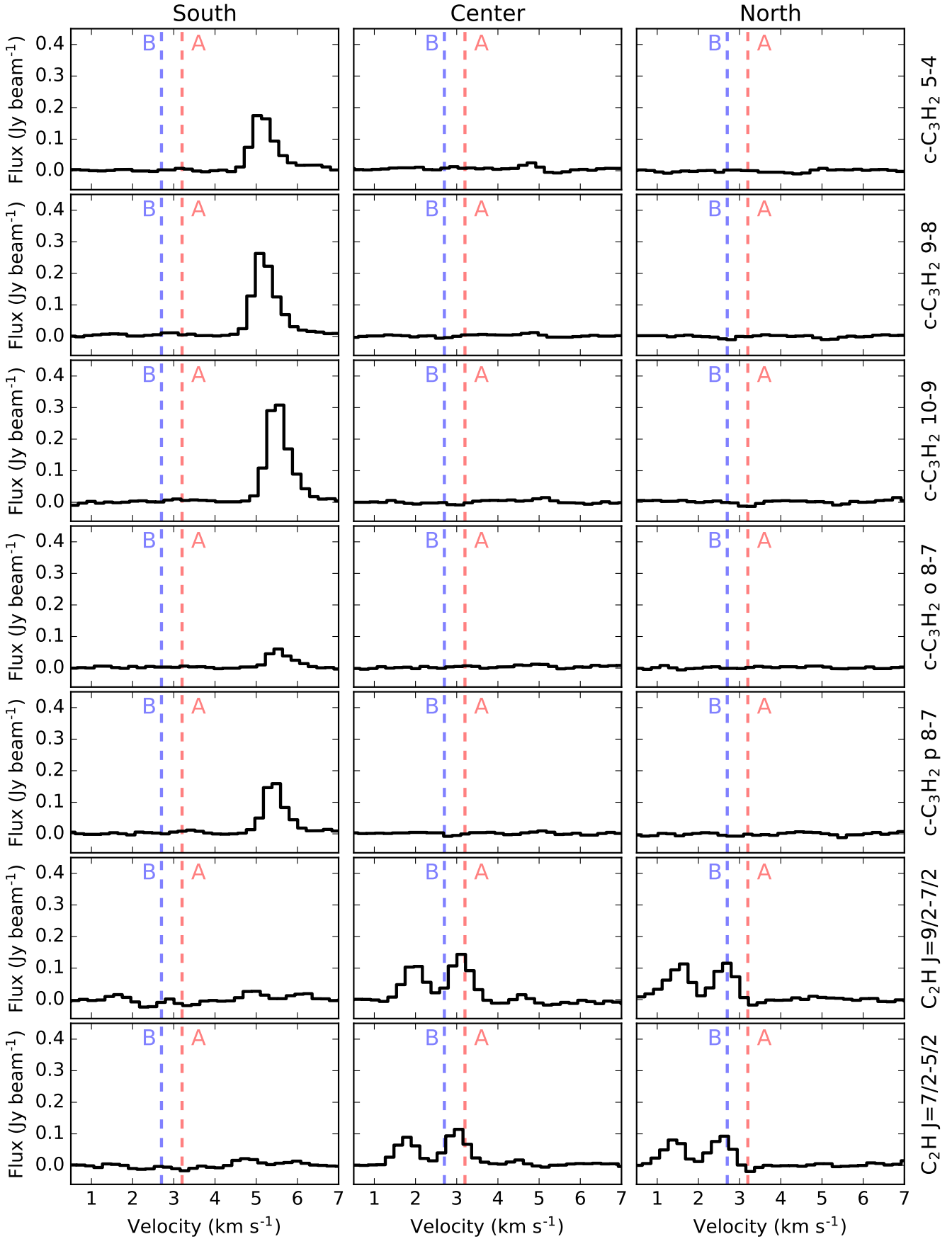


Fig. B.1. IRAS 16293–2422 ALMA spectra for all transitions of $c\text{-C}_3\text{H}_2$ and C_2H for each of the south, center, and north positions shown in Fig. 3. The systemic velocities of sources A and B are marked with the vertical dashed lines. The anti-correlation of $c\text{-C}_3\text{H}_2$ and C_2H is also evident in the spectra shown here.

Appendix C: Peak intensities and line ratios
Table C.1. c-C₃H₂ and C₂H peak intensities.

Molecules	c-C ₃ H ₂					C ₂ H			
	5–4	9–8	10–9	8 _{2,6} –7 _{3,5}	8 _{3,6} –7 _{2,5}	$J = 9/2-7/2 F = 5-4$	$J = 9/2-7/2 F = 4-3$	$J = 7/2-5/2 F = 4-3$	$J = 7/2-5/2 F = 3-2$
IRAS 16293–2422 (rms = 10 mJy beam ⁻¹)									
South ^a	240	410	350	90	200	30	30	30	30
Center ^a	30	30	30	30	30	170	140	140	110
North ^a	30	30	30	30	30	150	130	110	110
VLA 1623–2417 – APEX (rms = 80 mK)									
A	960	616	680	342

Notes. ^(a)For the positions with nondetections, three times the rms noise is used for the calculations.

Table C.2. N₂H⁺ and N₂D⁺ parameters for VLA 1623–2417.

Parameter	Observed			
	N ₂ H ⁺ 1–0 ^a	N ₂ H ⁺ 6–5 ^b	N ₂ D ⁺ 1–0 ^a	N ₂ D ⁺ 2–1 ^a
T_{mb} (K)	3.3 ± 0.1	0.2 ± 0.1	0.57 ± 0.1	1.5 ± 0.2
$\Delta v_{\text{single dish}}$ (km s ⁻¹)	0.56 ± 0.005	0.7 ± 0.2	0.55 ± 0.032	0.55 ± 0.009
η_{mb}	0.95	0.63	0.95	0.94
Ω_{beam} (″)	26.5	36	32.1	16.3
Ratio	0.06 ± 0.03		2.6 ± 0.6	
Column density (cm ⁻²)	1.3 × 10 ¹³		1.8 × 10 ¹²	
H ₂ density (cm ⁻³)	5 × 10 ⁷ –7 × 10 ⁹		5 × 10 ⁷ –7 × 10 ⁹	
T_{ex} (K)	11–12		11–12	
$\Omega_{\text{source}} = \Omega_{\text{beam}}$	N ₂ H ⁺ 4–3		N ₂ D ⁺ 3–2	
$I_{\nu, \text{predicted}}$ (mJy beam ⁻¹)	99		22	
$\Omega_{\text{beam, obs}}$ (″)	0.85		0.76	
σ_{obs} (mJy beam ⁻¹)	94.9		8.58	
S/N	1		2.6	
$\Omega_{\text{source}} = 1''$	N ₂ H ⁺ 4–3		N ₂ D ⁺ 3–2	
$I_{\nu, \text{predicted}}$ (mJy beam ⁻¹)	2631		364	
$\Omega_{\text{beam, obs}}$ (″)	0.85		0.76	
σ_{obs} (mJy beam ⁻¹)	94.9		8.58	
S/N	27		42	

Notes. ^(a)IRAM 30 m observations from [Punanova et al. \(2016\)](#). ^(b)*Herschel* observations from [Favre et al. \(2017\)](#).

The observed peak intensities of C₂H and c-C₃H₂ are listed in this appendix (Table C.1). The peak intensities are used in Sects. 4.2 and 4.3. In addition, the detailed calculation of expected peak intensities for N₂H⁺ and N₂D⁺ are also summarized here (Table C.2).

Single-dish observations of low- J transitions of CN, HCN, and HNC show strong detections relative to other embedded systems ([Jørgensen et al. 2004](#)). Our recent APEX observations also detected NO toward VLA 1623. However, single-dish observations of NH₃ ([Wootten et al. 1994](#); [Liseau et al. 2003](#)) and N₂H⁺ ([Liseau et al. 2015](#); [Punanova et al. 2016](#)) indicate that these molecules have very low abundances at the position of VLA 1623. N₂D⁺ also exhibits the same behavior ([Punanova et al. 2016](#)). Furthermore, *Herschel* observations of high- J N₂H⁺ toward VLA 1623 ([Liseau et al. 2015](#); [Favre et al. 2017](#)) show that the molecule is detected up to the $J = 6-5$ transition peaking at ~0.1 K km s⁻¹ but the emission is extended. The observed parameters of N₂H⁺ and N₂D⁺ from [Punanova et al. \(2016\)](#) and [Favre et al. \(2017\)](#) are listed in Table C.2.

Using the observed transitions of N₂H⁺ and N₂D⁺, we derive the density and excitation temperature with the method described

in Sect. 4.1. The different beam sizes of the observations require a beam dilution correction factor that is given by $T'_{\text{mb}} = T_{\text{mb, obs}} \frac{\Omega_{\text{beam}}}{\Omega_{\text{source}}}$, where T'_{mb} and $T_{\text{mb, obs}}$ are the corrected and observed main beam temperature, respectively, Ω_{beam} is the solid angle of the single-dish beam and Ω_{source} is the solid angle subtended by the source. We assume the emission is concentrated in the region of the smaller beam, which would be of 26.5″ for N₂H⁺ and 16.3″ for N₂D⁺.

To compare with our ALMA observations, the expected peak for N₂H⁺ 4–3 and N₂D⁺ 3–2 is derived from the observations of [Punanova et al. \(2016\)](#) and [Favre et al. \(2017\)](#). The N₂H⁺ molecular data file without hyperfine structure is used to calculate the kinetic temperature of both molecules. The collisional rate coefficients for N₂H⁺ are taken to be the same as HCO⁺ ([Botschwina et al. 1993](#)) and extrapolated ([Schöier et al. 2005](#)). Since LAMDA does not have a molecular data file for N₂D⁺, the data file for N₂H⁺ is used, selecting the corresponding transition rather than frequency. For the predicted peak emissions for N₂H⁺ 4–3 and N₂D⁺ 3–2, two cases are examined: (i) the observed emission is evenly distributed in the single-dish beam (i.e., beam-filling factor = 1) and (ii) the emission is

concentrated in a $1''$ region (i.e., beam filling factor < 1). The second case introduces a beam dilution correction. The results of the calculation are listed in Table C.2.

The kinetic temperature and number density obtained in our calculations (~ 11 K, $\sim 10^{7-9}$ cm $^{-3}$) are slightly higher than those previously reported (7.7 K, 10^6 cm $^{-3}$; Punanova et al. 2016). The column densities, however, are similar to those reported in Punanova et al. (2016). For N $_2$ H $^+$, our results are also consistent with those reported in Liseau et al. (2015).

Since only one transition of N $_2$ D $^+$ toward IRAS 16293 is presented here, the physical parameters of other molecules are used to derive its column density. Using the physical parameters obtained from the DCO $^+$ 5–4/3–2 ratio (Sect. 4.1 and Table 4), we calculated a column density of $1.5\text{--}2 \times 10^{13}$ cm $^{-2}$ for N $_2$ D $^+$. If instead we used the physical parameters obtained from the

N $_2$ D $^+$ observations toward VLA 1623, we find a column density of $4\text{--}5 \times 10^{13}$ cm $^{-2}$ for N $_2$ D $^+$ 3–2 toward IRAS 16293. For both sets of parameters, the column density is higher by one order of magnitude in comparison to the N $_2$ D $^+$ toward VLA 1623.

Appendix D: PILS full spectra

The PILS survey spectra (Jørgensen et al. 2016) is reproduced here for the south c–C $_3$ H $_2$ peak position and at one beam away from the position of IRAS 16293 B. Figures D.1–D.3 present the full spectra for both positions. At the south c–C $_3$ H $_2$ peak position, the spectra is multiplied by a factor of 10 to bring out the features. Few molecular lines are detected at this position, apart from common molecules like HCO $^+$ and CO, only c–C $_3$ H $_2$ and H $_2$ CS are detected.

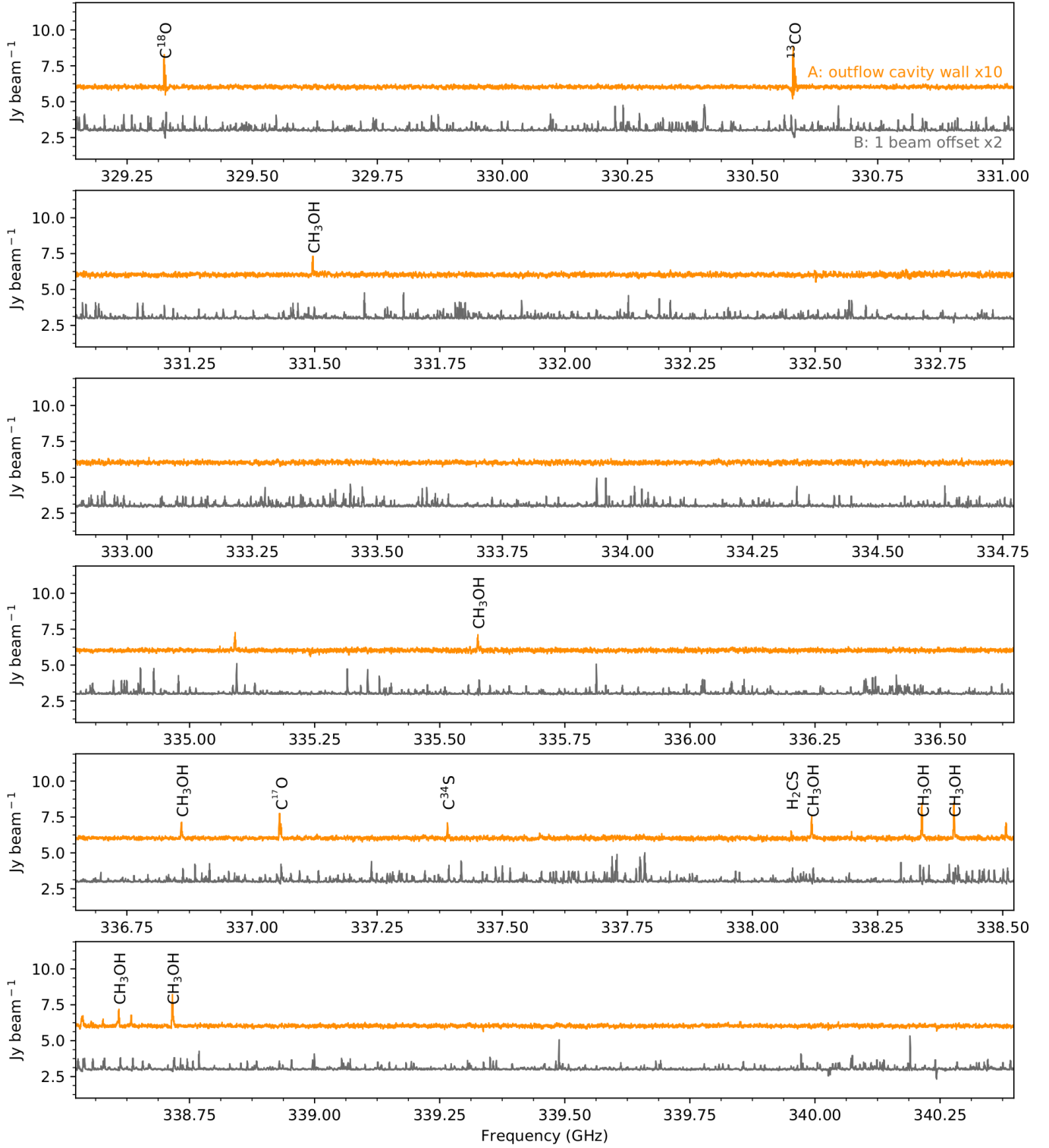


Fig. D.1. Full spectra obtained in the PLS survey for IRAS 16293–2422. Here, the frequency range 329.15–340.4 GHz is shown. The rest of the spectra is shown in Figs. D.2 and D.3. The spectra for the IRAS 16293–2422 B is one beam away from the source position ($\alpha_{J2000} = 16:32:22.581$, $\delta_{J2000} = -24:28:32.80$), we note that it is multiplied by a factor of 2. The spectra for IRAS 16293–2422 A’s outflow cavity wall is centered at the observed peak of $c\text{-C}_3\text{H}_2$ ($\alpha_{J2000} = 16:32:22.867$, $\delta_{J2000} = -24:28:39.60$), we note that it is multiplied by a factor of 10 and shows very little emission other than $c\text{-C}_3\text{H}_2$, CH_3OH , CS , H_2CS , HCN , H_2CO , and HCO^+ .

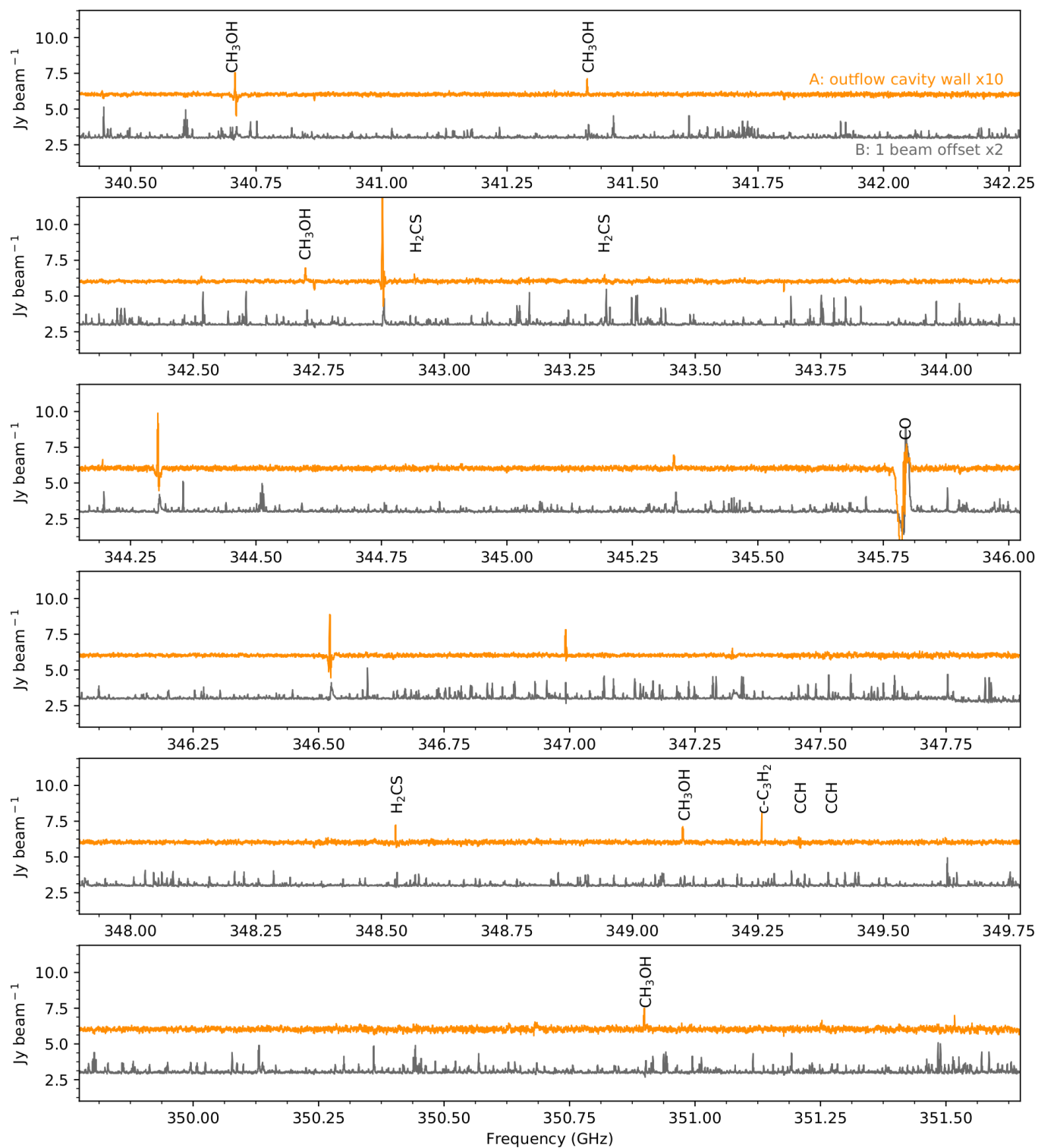


Fig. D.2. Same as in Fig. D.1 but for the frequency range 340.4–351.65 GHz. C_2H is marked for reference.

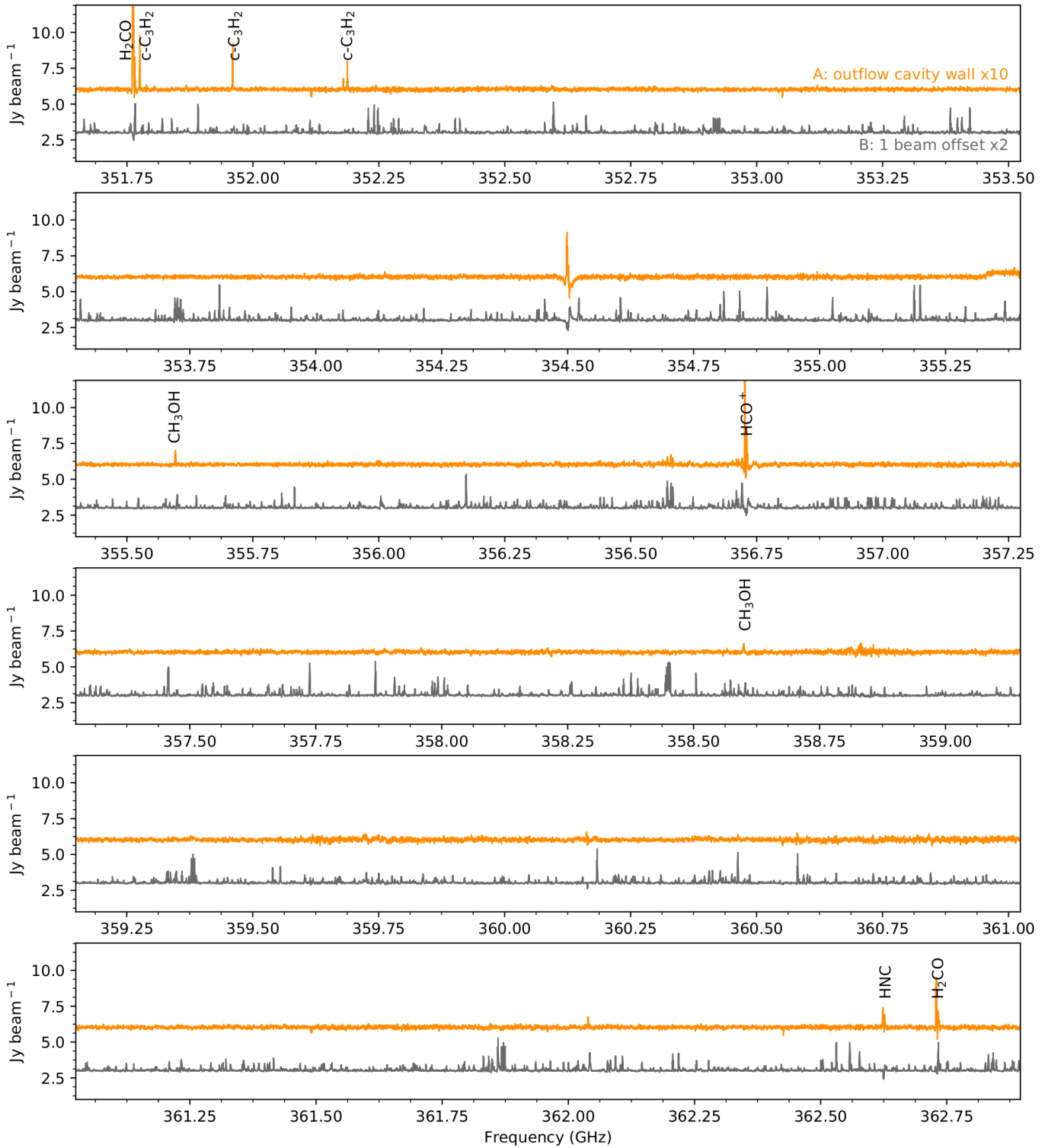


Fig. D.3. Same as in Fig. D.1 but for the frequency range 351.65–362.9 GHz.